6-30-2020

Atrx Deletion in Neurons Leads to Sexually Dimorphic Dysregulation of miR-137 and Spatial Learning and Memory Deficits.

Renee J. Tamming

Vanessa Dumeaux

Yan Jiang

Sarfraz Shafiq

Luana Langlois

See next page for additional authors
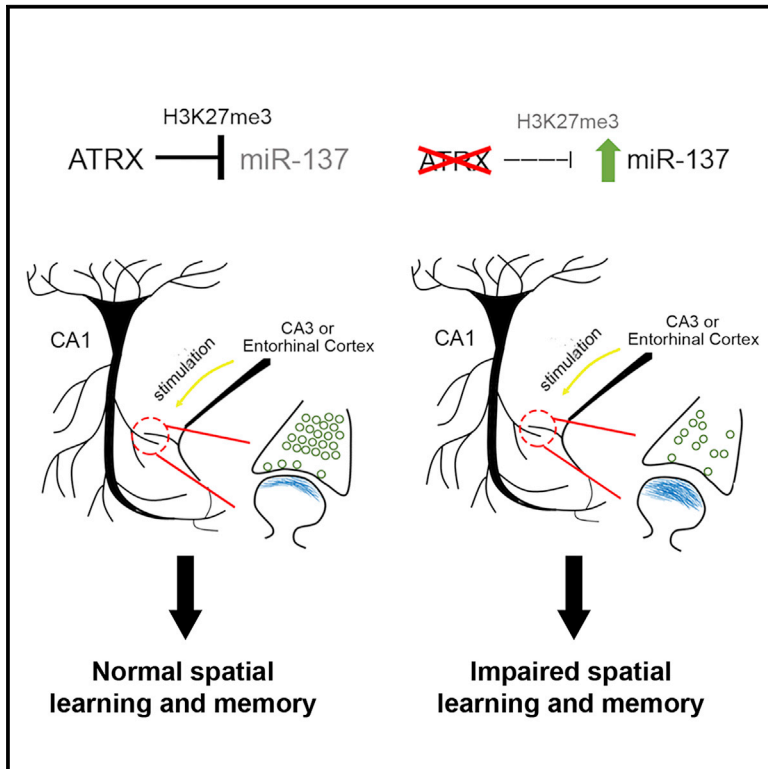
Authors

Renee J. Tamming, Vanessa Dumeaux, Yan Jiang, Sarfraz Shafiq, Luana Langlois, Jacob Ellegood, Lily R. Qiu, Jason P. Lerch, and Nathalie G. Bérubé

Atrx Deletion in Neurons Leads to Sexually Dimorphic Dysregulation of miR-137 and Spatial Learning and Memory Deficits

Graphical Abstract

Highlights

- Loss of ATRX in neurons has sexually dimorphic effects on long-term spatial memory

- Targeted deletion of neuronal ATRX in mice causes ultrastructural synaptic defects

- ATRX null neurons show sex-specific changes in miR-137 and target synaptic transcripts

- ATRX directly binds and suppresses miR-137 in males via enrichment of H3K27me3

Authors

Renee J. Tamming, Vanessa Dumeaux, Yan Jiang, ..., Lily R. Qiu, Jason P. Lerch, Nathalie G. Bérubé

Correspondence

nberube@uwo.ca

In Brief

Targeted ablation of the ATRX intellectual disability gene in forebrain excitatory neurons of mice causes male-specific deficits in long-term spatial memory. Tamming et al. establish that ATRX suppresses miR-137 to regulate an ensemble of genes required to maintain synaptic integrity in the hippocampus.

Article

Atrx Deletion in Neurons Leads to Sexually Dimorphic Dysregulation of miR-137 and Spatial Learning and Memory Deficits

Renee J. Tamming,[1,2,3] Vanessa Dumeaux,[4,7] Yan Jiang,[1,2] Sarfraz Shafiq,[1,4,5] Luana Langlois,[1,2,5] Jacob Ellegood,[8]
Lily R. Qiu,[8,10] Jason P. Lerch,[8,9,10] and Nathalie G. Bérubé[1,2,4,5,6,11,*]
[1]Children's Health Research Institute, London, ON, Canada
[2]Lawson Health Research Institute, London, ON, Canada
[3]Department of Biochemistry, Western University, London, ON, Canada
[4]Department of Paediatrics, Western University, London, ON, Canada
[5]Department of Anatomy & Cell Biology, Western University, London, ON, Canada
[6]Department of Oncology, Western University, London, ON, Canada
[7]PERFORM Centre, Concordia University, Montreal, QC, Canada
[8]Mouse Imaging Centre, The Hospital for Sick Children, Toronto, ON, Canada
[9]Department of Medical Biophysics, The University of Toronto, Toronto, ON, Canada
[10]Wellcome Centre for Integrative Neuroimaging, The University of Oxford, Oxford, UK
[11]Lead Contact
*Correspondence: nberube@uwo.ca
https://doi.org/10.1016/j.celrep.2020.107838

SUMMARY

ATRX gene mutations have been identified in syndromic and non-syndromic intellectual disabilities in humans. ATRX is known to maintain genomic stability in neuroprogenitor cells, but its function in differentiated neurons and memory processes remains largely unresolved. Here, we show that the deletion of neuronal *Atrx* in mice leads to distinct hippocampal structural defects, fewer presynaptic vesicles, and an enlarged postsynaptic area at CA1 apical dendrite-axon junctions. We identify male-specific impairments in long-term contextual memory and in synaptic gene expression, linked to altered miR-137 levels. We show that ATRX directly binds to the *miR-137* locus and that the enrichment of the suppressive histone mark H3K27me3 is significantly reduced upon the loss of ATRX. We conclude that the ablation of ATRX in excitatory forebrain neurons leads to sexually dimorphic effects on miR-137 expression and on spatial memory, identifying a potential therapeutic target for neurological defects caused by ATRX dysfunction.

INTRODUCTION

α-Thalassemia X-linked mental retardation (ATR-X) syndrome is a rare congenital X-linked disorder resulting in moderate to severe intellectual disability (ID), developmental delay, microcephaly, hypomyelination, and a mild form of α-thalassemia (OMIM: 301040) (Gibbons et al., 1995). In a recent study of ~1,000 individuals with ID, *ATRX* mutations were identified as one of the most frequent causes of non-syndromic ID (Grozeva et al., 2015), emphasizing a key requirement for this gene in cognitive processes. ATRX-related ID arises from hypomorphic mutations in the *ATRX* gene, most commonly in the highly conserved ATRX/DNMT3/DNMT3L and Switch/Sucrose non-fermenting domains (Gibbons et al., 1997, 2008). The former targets ATRX to chromatin by means of a histone reader domain that recognizes specific histone tail modifications (Eustermann et al., 2011), and the latter confers ATPase activity and is critical for its chromatin remodeling activity (Lewis et al., 2010; Picketts et al., 1996).

ATRX, in a complex with the histone chaperone death domain-associated protein (DAXX), promotes the deposition of the histone variant H3.3 at heterochromatic domains, including telomeres and pericentromeres (Goldberg et al., 2010; Law et al., 2010). However, ATRX is also required for the deposition of H3.3 within the gene body of a subset of G-rich genes, to reduce G-quadruplex formation, and to promote transcriptional elongation (Levy et al., 2015). ATRX is also required for the postnatal suppression of a network of imprinted genes in the neonatal brain by promoting long-range chromatin interactions via CCCTC-binding factor (CTCF) and cohesin (Kernohan et al., 2010).

In mice, germline deletion of *Atrx* results in embryonic lethality (Garrick et al., 2006), while conditional deletion of *Atrx* in neuroprogenitors leads to excessive DNA damage caused by DNA replication stress and subsequent Tp53-dependent apoptosis (Seah et al., 2008; Watson et al., 2013). Mice with the deletion of exon 2 of *Atrx* (*Atrx*^(ΔE2)) were generated that result in the global reduction of *Atrx* expression. These mice are viable and exhibit
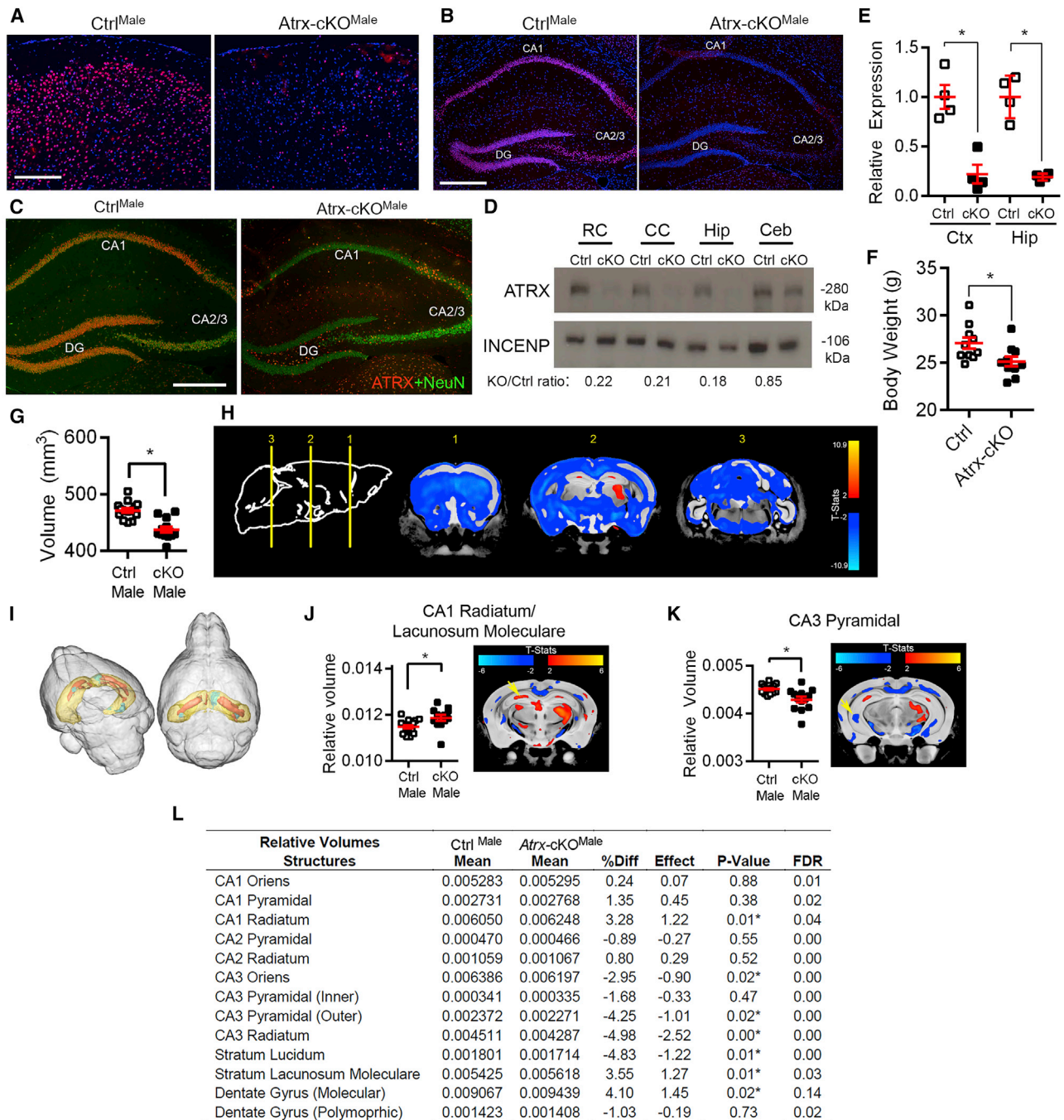
Figure 1. Neuronal Inactivation of *Atrx* in Atrx-cKO^Male Mice Causes Altered Hippocampal Morphology

(A and B) Immunofluorescence of the cortex (A) and hippocampus (B) of Ctrl^Male and Atrx-cKO^Male mice. Scale bar: 100 μm for cortex, 200 μm for hippocampus.

(C) Co-staining of ATRX (red) and NeuN (green) shows absence of ATRX in hippocampal neurons in Atrx-cKO^Male mice. CA1: cornu ammonis 1, CA2: cornu ammonis 2, CA3: cornu ammonis 3, DG: dentate gyrus. Scale bar: 200 μm.

(D) Western blot of ATRX in rostral cortex (RC), caudal cortex (CC), hippocampus (Hip), and cerebellum (Ceb) of Ctrl^Male and Atrx-cKO^Male mice. The fold change in protein expression normalized to INCENP (loading control) is indicated below.

(E) *Atrx* RNA transcripts were measured by qRT-PCR in the rostral cortex (Ctx) ($p < 0.005$) and hippocampus (Hip) ($p < 0.001$) (n = 4 of each genotype).

(F) Body weight of Ctrl^Male and Atrx-cKO^Male mice at 3 months of age (n = 10 each genotype; $p < 0.05$ by unpaired Student's t test). MRI of 16 Ctrl^Male and 13 *Atrx*-cKO^Male fixed mouse brains.

(G) Absolute total volume of Ctrl^Male and *Atrx*-cKO^Male mouse brains ($p < 0.0001$).

(H) Coronal views of Ctrl^Male and *Atrx*-cKO^Male brains show changes in the density of absolute volume.

(legend continued on next page)

impaired novel object recognition memory, spatial memory in the Barnes maze, and contextual fear memory (Shioda et al., 2011). Molecular defects identified in these mice included decreased activation of calcium/calmodulin-dependent protein kinase II (CaMKII) and the α-amino-3-hydroxy-5-methyl-4-isoxazolepropionic acid (AMPA) receptor in the hippocampus, decreased spine density in the medial prefrontal cortex, and altered DNA methylation and increased expression of *Xlr3b* in neurons (Shioda et al., 2018). Our group also reported similar behavioral impairments in female mice that exhibit a mosaic expression of ATRX in the central nervous system (Tamming et al., 2017). However, the contribution of different cell types and sex differences to behavioral abnormalities has not yet been resolved.

To address these questions, we deleted *Atrx* in glutamatergic neurons of male and female mice. This approach bypasses the deleterious effects of the ATRX loss of function that we previously observed during brain development caused by replication stress in proliferating neuroprogenitors (Garrick et al., 2006; Watson et al., 2013). A comprehensive analysis of these mice reveals that ATRX loss impairs long-term spatial learning and memory associated with morphological and synaptic ultrastructural changes in the hippocampus. We show that female mice lacking ATRX in neurons are protected from spatial learning and memory defects and identify sex-specific effects of ATRX loss on the expression of synaptic transcripts and miR-137. Overall, we identify a sex-specific function for ATRX in neurons in the regulation of long-term spatial memory associated with abnormal synapse ultrastructure.

RESULTS

Generation of Atrx-cKO[Male] Mice

We generated mice lacking ATRX in postnatal forebrain excitatory neurons using Cre/loxP-mediated recombination of the *Atrx* gene with the *CaMKII*-Cre driver line of mice (Tronche et al., 1999). Immunofluorescence staining of control (Ctrl[Male]) and knockout (*Atrx*-cKO[Male]) brain cryosections obtained from 3-month-old male mice confirms the loss of ATRX protein in the cortex and hippocampus (Figures 1A and 1B). Co-staining for ATRX and the neuronal marker NeuN shows that ATRX is highly expressed in the hippocampal neurons of the CA1, CA2/3, and dentate gyrus, but is absent in these cells in *Atrx*-cKO[Male] mice (Figure 1C). Western blot analysis demonstrates that ATRX protein is reduced by ~80% in the rostral and caudal cortices and the hippocampus (Figure 1D). qRT-PCR shows that *Atrx* transcript levels are decreased by 78% (±9.4%) and 81% (±1.7%) in the cortex and hippocampus, respectively (Figure 1E). *Atrx*-cKO[Male] mice survive to adulthood but exhibit reduced body weight (Figure 1F).

Magnetic Resonance Imaging (MRI) Analysis Identifies Anatomical Abnormalities in the Hippocampus of Atrx-cKO[Male] Mice

A T2-weighted MRI sequence from 16 Ctrl[Male] and 13 *Atrx*-cKO[Male] mice shows that the overall volume of the *Atrx*-cKO[Male] brain is significantly smaller compared to controls (92.8% of control volume, $p < 0.0001$; Figure 1G) and cumulative serial slices (Figure 1H) correlated with smaller body size. We thus examined hippocampal neuroanatomy relative to total brain volume (Figure 1I). The relative volumes of the CA1 stratum radiatum (SR) and the stratum lacunosum moleculare (SLM) were significantly increased in *Atrx*-cKO[Male] mice compared to controls (Figure 1J), whereas the CA3 pyramidal layer volume was significantly decreased (Figure 1K). Relative volumes of all hippocampal regions are tabulated in Figure 1L.

We postulated that the increase in the relative volume of the CA1 SR and SLM may be due to increased length or branching of CA1 apical dendrites. To investigate this possibility, we used Golgi staining to sporadically label neurons (Figure S1A), and Sholl analysis was performed using confocal microscopy images to evaluate apical dendrite branching of CA1 hippocampal neurons. Dendritic branching and length were not significantly different between Ctrl[Male] and *Atrx*-cKO[Male] CA1 neurons (Figures S1B–S1G). Quantification of astrocytes (GFAP+) and microglia (IBA1+) and total number of cells (inferred from DAPI+ staining) identified no difference between *Atrx*-cKO[Male] and control hippocampi (Figures S1H–S1J). Overall, the increased relative volume of the CA1 SR and SLM cannot be explained by increased length or complexity of dendritic trees or by an increased number of cells.

Pre- and Postsynaptic Ultrastructural Defects in the CA1 Apical Dendritic Region of cKO[Male] Mice

Based on the hippocampal alterations detected by MRI, we wanted to see whether we could detect ultrastructural changes in the CA1 SR-SLM area. Images of synapses were obtained by transmission electron microscopy (TEM) and various measurements performed (Figure 2A). The spatial distribution of vesicles in relation to the cleft was not significantly different between *Atrx*-cKO[Male] and Ctrl[Male] synapses (Figure 2B). However, the total number of vesicles, the density of the vesicles, and the number of docked vesicles was significantly decreased at *Atrx*-cKO[Male] synapses (Figures 2C–2E). We also found that the size of the postsynaptic density (PSD) and the width of the synaptic cleft were both significantly increased (Figures 2F and 2G), whereas the length of the active zone, cluster size, or diameter of the vesicles did not vary significantly (Figures 2H–2J). These

---

(I) Cumulative 3-dimensional (3D) image generated from Ctrl[Male] and *Atrx*-cKO[Male] mouse brains reveals altered hippocampal volume relative to brain size. Hippocampus is yellow, areas of increased volume in *Atrx*-cKO[Male] are orange, and areas of decreased volume are green.

(J) Relative volume of CA1 stratum radiatum and lacunosum moleculare between Ctrl[Male] and *Atrx*-cKO[Male] mice ($p < 0.05$). MRI image at right shows cumulative changes in *Atrx*-cKO[Male] compared to Ctrl[Male] mice.

(K) Relative size of CA3 pyramidal layer between Ctrl[Male] and *Atrx*-cKO[Male] mice ($p < 0.005$). MRI image at right shows cumulative changes in *Atrx*-cKO[Male] mice compared to controls.

(L) Relative volumes of all hippocampal structures, including mean and standard deviation of Ctrl[Male] and *Atrx*-cKO[Male], percentage difference (%Diff), effect size, p value, and false discovery rate (FDR). Asterisks indicate $p < 0.05$.
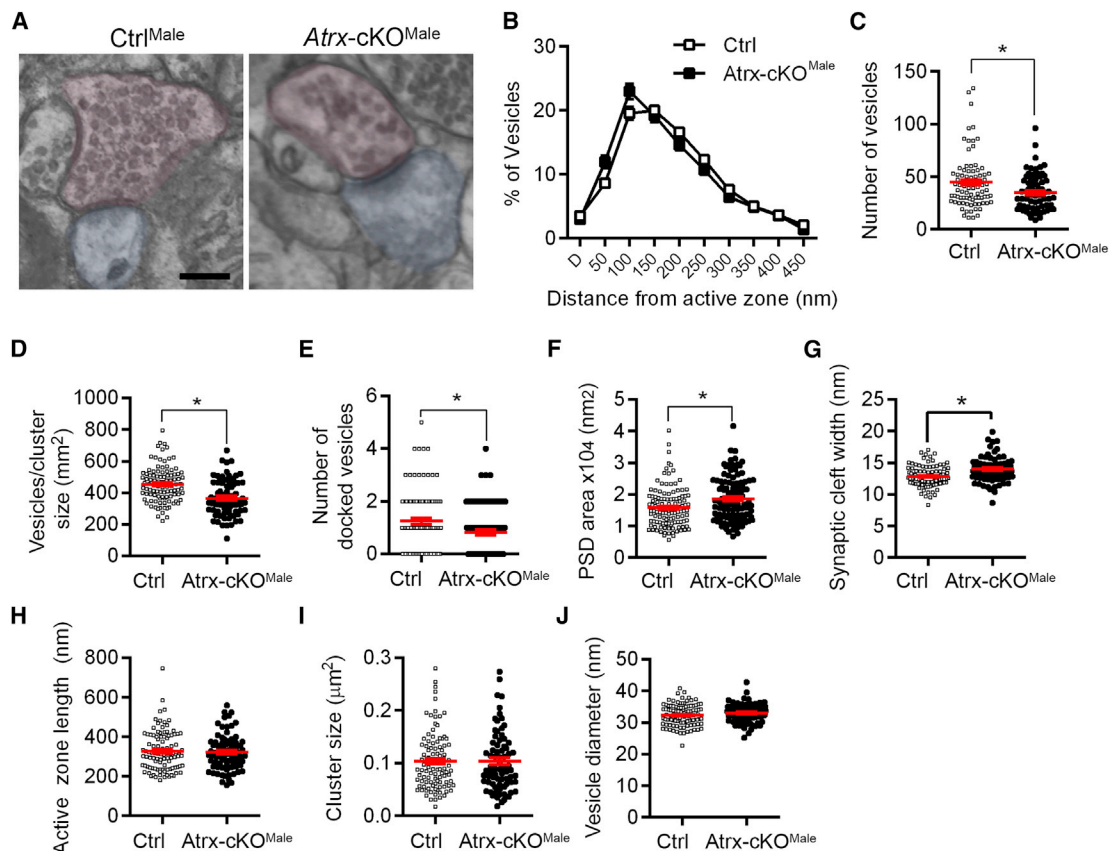
See also Figure S1.

Figure 2. Ultrastructural Analysis of Atrx-cKO[Male] CA1 Apical Synapses

(A) Representative images of Ctrl[Male] and Atrx-cKO[Male] CA1 synapses imaged by transmission electron microscopy. Red indicates presynaptic bouton, and the postsynaptic spine is blue. Scale bar, 200 nm.

(B) Number of vesicles in 50-nm bins from the active zone (p = 0.95).

(C) Number of total vesicles (p < 0.01).

(D) Density of vesicles per cluster (p < 0001).

(E) Number of docked vesicles (p < 0.05).

(F) Area of the postsynaptic density (PSD) (p < 0.005).

(G) Synaptic cleft width (p < 0.0001).

(H) Length of the presynaptic active zone (p = 0.70).

(I) Synaptic vesicle cluster size (p = 0.99).

(J) Vesicle diameter (p = 0.19).

All of the data in (B)–(J) were obtained from 104 Ctrl[Male] synapses and 84 Atrx-cKO[Male] synapses from 3 brains of each genotype. The data were analyzed by unpaired Student's t test (C–J) or 2-way repeated-measures ANOVA with Sidak's multiple comparisons test (B). The data are displayed as means ± SEMs in (B)–(J).

results reveal that ATRX is required for the structural integrity of the pre- and postsynapse, including maintenance of the synaptic vesicle pool at presynaptic termini and potential defects in postsynaptic protein clustering.

Atrx Deletion in Excitatory Neurons Causes Spatial Learning and Memory Deficits

We then performed behavior tests on Ctrl[Male] and Atrx-cKO[Male] mice. Locomotor activity in the open field test was not significantly different between the two genotypes, either over time (F = 0.17, p = 0.68) or when considering total distance traveled (T = 0.67, p = 0.51; Figures S2A and S2B). The Atrx-cKO[Male] mice did not spend more time in the center of the chamber

over time (F = 2.96, p = 0.09; Figure S2C). However, they spent significantly more total time in the center of the chamber compared to controls (T = 2.26, p = 0.03; Figure S2D), indicating that the loss of ATRX in neurons has an anxiolytic effect. This result was confirmed by the behavior of the Atrx-cKO[Male] mice in the elevated plus maze, where they spent significantly more time in the open arm of the maze compared to controls (T = 2.16, p = 0.04; Figure S2E). We observed no difference in percentage of alternation in the Y maze (T = 0.94, p = 0.35; Figure S2F), nor in the training phase of the novel object recognition task (Ctrl[Male] T = 1.13, p = 0.27; Atrx-cKO[Male] T = 1.66, p = 0.11; Figure S2G) or memory tests at 1.5 h (Ctrl[Male] T = 4.28, p < 0.001; Atrx-cKO[Male] T = 3.55, p < 0.005) or 24 h (Ctrl[Male]T = 1.65,

p = 0.11; $Atrx$-cKO^{Male} T = 2.46, p < 0.05) following training (Figure S2H).

To investigate the effects of ATRX ablation on spatial learning and memory, we tested the mice in the Morris water maze task. The $Atrx$-cKO^{Male} mice exhibited a significant increase in latency to find the platform on day 3 of the learning portion of the task compared to controls; however, by day 4, they were able to find the platform as quickly as control mice (F = 4.62, p = 0.04; Figure 3A). This finding was reflected in the distance traveled to find the platform (F = 4.83, p = 0.04; Figure 3B). Swim speed was comparable to controls over the 4 days of learning the task (F = 0.04, p = 0.84; Figure 3C). Memory was tested on day 5 (24 h after the last training day) and day 12 (7 days after the last training day). On day 5, both Ctrl^{Male} mice (F = 29.36, p < 0.0001) and the $Atrx$-cKO^{Male} mice (F = 18.97, p < 0.0001) spent significantly more time in the target quadrant than the left, opposite, or right quadrants, signifying intact spatial memory (Figure 3D). However, on day 12, the $Atrx$-cKO^{Male} mice did not spend significantly more time in the target quadrant (F = 1.42, p = 0.26), whereas controls mice did (F = 6.79, p < 0.01), suggesting a long-term spatial memory deficit (Figure 3E). $Atrx$-cKO^{Male} mice froze significantly less in the contextual fear memory task in comparison to their control counterparts 24 h after a foot shock (over time F = 5.39, p = 0.03; total time T = 2.32; p = 0.03; Figures 3F and 3G). From these results, we conclude that neuronal ATRX is required in male mice for long-term hippocampal-dependent spatial memory.

Neuron-Specific Deletion of Atrx in Female Mice Does Not Cause Memory Deficits

To determine whether the loss of ATRX in female mice would cause similar behavioral defects, we generated $Atrx$-cKO female mice ($Atrx$-cKO^{Fem}) by mating $Atrx^{f/f}$ female mice to $Atrx^{f/Y}$;Cam-KIICre$^{+/-}$ male mice. The $Atrx$-cKO^{Fem} progeny from this cross survived to adulthood, had a normal appearance, and did not display any overt behavioral defects. We verified $Atrx$ deletion by immunofluorescence staining and qRT-PCR (Figures S3A–S3C). In the open field test, $Atrx$-cKO^{Fem} mice exhibit the same level of locomotion over time (F = 1.24, p = 0.28) and travel the same distance as the Ctrl^{Fem} mice (T = 1.11, p = 0.28; Figures S4A and S4B). Likewise, $Atrx$-cKO^{Fem} mice did not spend more time in the center during the open field test compared to control mice (over time F = 0.01, p = 0.93; total time T = 0.10, p = 0.93; Figures S4C and S4D), In the elevated plus maze, the $Atrx$-cKO^{Fem} mice spent a similar amount of time in the exposed open arm as control mice (T = 0.49, p = 0.63; Figure S4E), indicating that the decreased anxiety levels are specific to $Atrx$-cKO^{Male} mice.

$Atrx$-cKO^{Fem} had normal latency to reach the platform during the Morris water maze training sessions and traveled the same distance and at the same speed as Ctrl^{Fem} mice (latency F = 3.63, p = 0.07; distance F = 1.39, p = 0.25; speed F = 1.24, p = 0.28; Figures 3H–3J). Memory of the platform location remained equivalent to that of controls when tested on probe day 5 or probe day 12 (Ctrl^{Fem} day 5 F = 12.80, p < 0.0001; $Atrx$-cKO^{Male} day 5 F = 11.63, p < 0.001; Ctrl^{Fem} day 12 F = 16.47, p < 0.0001; $Atrx$-cKO^{Fem} day 12 F = 12.97, p < 0.0001; Figures 3K and 3L). Finally, there was no difference in freezing behavior between

Ctrl^{Fem} and $Atrx$-cKO^{Fem} 24 h after foot shock in the contextual fear-conditioning task (over time F = 0.02, p = 0.88; total time T = 0.15, p = 0.88; Figures 3M and 3N).

We also compared the data obtained in female and male mice to determine whether there are sex or genotype effects. There is no effect of genotype, but a significant effect of sex in total distance traveled (p = 0.0001) and time spent in the center (p < 0.0001) during the open field test, as female mice traveled a shorter distance and spent less time in the center than male mice (Figures S5A and S5B). A Sidak post hoc multi-comparison test identifies significantly increased time spent in the center area for the $Atrx$-cKO^{Male} mice. Analysis of the time spent in the target quadrant during the day 12 probe test of the Morris water maze finds no effect of sex or genotype (2-way ANOVA, p = 0.08; Figure S5C). In the fear conditioning test, we identified a sex effect but not a genotype effect (2-way ANOVA, p = 0.0002 and p = 0.09, respectively) in which female mice spent less time freezing at the 24 hour time point compared to male mice. Applying a post hoc multi-comparison test shows that $Atrx$-cKO^{Male} mice spent significantly more time freezing than did same sex controls (Figure S5D). We conclude from these results that male mice behave differently from female mice regardless of genotype in the open field test and in the fear conditioning task and that ATRX loss in forebrain excitatory neurons does not affect learning and memory in female mice, at least in the tests performed here.

Impaired Object Location Associative Memory in the Rodent Version of the Paired-Associate Learning (dPAL) Task

Given the male-specific defects in spatial memory, we performed additional cognitive tasks on the $Atrx$-cKO^{Male} and Ctrl^{Male} mice. The dPAL touchscreen task in mice is analogous to cognitive testing done in humans by the Cambridge Neuropsychological Test Automated Battery (CANTAB) (Nithianantharajah et al., 2015; Sahakian et al., 1988), and normal performance on this task is thought to depend in part on the hippocampus (Delotterie et al., 2015; Kim et al., 2015).

Ctrl^{Male} and $Atrx$-cKO^{Male} mice were trained to identify the position of three images as depicted in Figure 4A by undergoing 36 trials per day for 10 weeks. The results demonstrate that the $Atrx$-cKO^{Male} mice exhibit a profound deficit in this task, indicated by both the percentage of correct nose pokes (F = 10.53, p < 0.01; Figure 4B) and the number of correction trials required (F = 30.64, p < 0.0001; Figure 4C; Videos S1 and S2). These defects could not be attributed to an inability to perform within the chamber or to attentional deficits, as latencies to a correct answer (F = 0.48, p = 0.49), to an incorrect answer (F = 0.13, p = 0.73), and to retrieve the reward (F = 0.98, p = 0.33) were not significantly different between Ctrl^{Male} and $Atrx$-cKO^{Male} mice (Figures 4D–4F). To determine whether the impairment in the dPAL task is caused by a vision problem rather than a learning defect, the mice were also tested in the visual paired discrimination (VPD) automated touchscreen task in which the mice must discriminate between two images regardless of their position on the screen. While the $Atrx$-cKO^{Male} mice took significantly longer to reach the criterion pretesting (T = 2.95, p < 0.01; Figure 4G), there was no difference in the percentage of correct
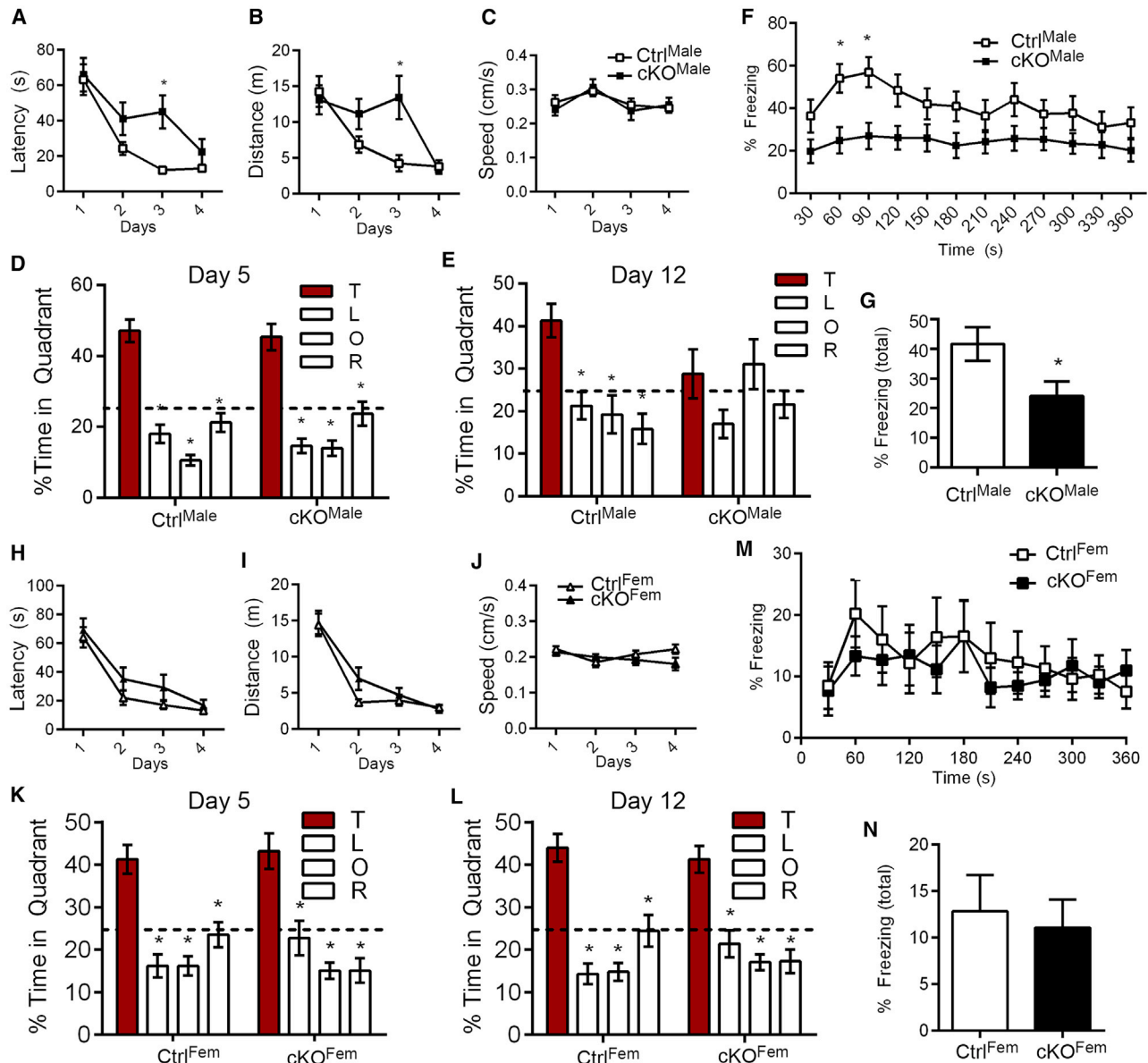
Figure 3. Sexually Dimorphic Impairment of Long-Term Spatial Memory upon Loss of Neuronal ATRX

(A) Latency to reach the platform in the Morris water maze ($p < 0.05$).

(B and C) Distance traveled ($p < 0.05$) (B), and swimming speed ($p = 0.84$) (C) over 4 days of training (4 trials/day) in the Morris water maze task (n = 15 each genotype).

(D and E) Time spent in each quadrant after removal of the platform on day 5 (D) and (E) on day 12 (E). The dotted lines indicate chance at 25% and asterisks indicate significant difference to the target (T) quadrant (n = 15 each genotype).

(F) Time freezing over 360 s during the contextual fear conditioning task ($p < 0.05$) (n = 22 each genotype).

(G) Total time freezing ($p < 0.05$) (n = 22 each genotype).

(H–J) Latency to reach the platform in the Morris water maze ($p = 0.07$) (H), distance traveled ($p = 0.25$) (I), and swimming speed ($p = 0.28$) (J) over 4 days of training (4 trials/day) in the Morris water maze (Ctrl[Fem] n = 15, Atrx-cKO[Fem] n = 12).

(K and L) Time spent in each quadrant after removal of the platform on probe day 5 (K) and on probe day 12 (L). The dotted line indicates chance at 25%.and asterisks indicate significant difference to the target (T) quadrant ($p < 0.05$).

(M) Time freezing ($p = 0.88$).

(N) Total time freezing during the contextual fear conditioning task ($p = 0.88$).

Statistics by two-way repeated-measures ANOVA with Sidak's multiple comparisons test was applied in (A)–(C), (F), (H)–(J) and (M). One-way ANOVA was applied in (D) and (E), (K), and (L). Student's t test was used for (G) and (N). See also Figures S2–S5.
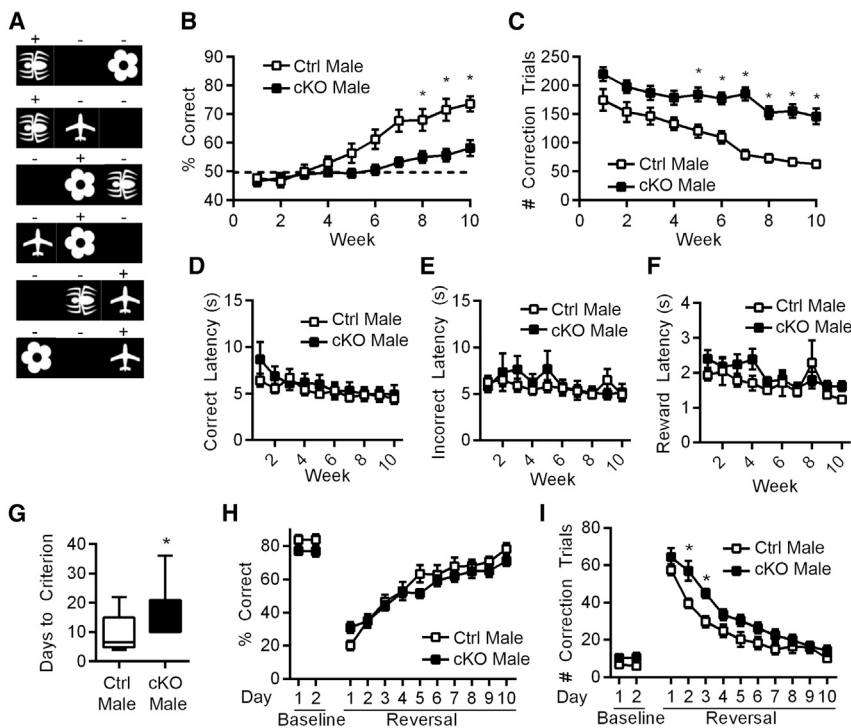
Figure 4. Atrx-cKO[Male] Mice Display Deficits in the Paired-Associate Operant Task

(A) Representative images used in the paired-associate learning task, in which touching the (+) stimuli on the screen results in reward and the (−) stimuli results in negative reinforcement (Talpos et al., 2009).
(B) Percentage correct over 10 weeks (p < 0.005). Dotted line indicates percentage correct by chance.
(C) Number of correction trials required over 10 weeks (p < 0.0001).
(D) Latency to choose a correct answer (p = 0.49).
(E) Latency to choose an incorrect answer (p = 0.72).
(F) Latency to retrieve the reward (p = 0.33).
(G) Number of days to reach criterion in the visual paired discrimination (VPD) task (p < 0.01).
(H) Percentage correct during baseline (2 days) and reversal (10 days) (p = 0.25).
(I) Number of correction trials required during baseline and reversal trials (p < 0.005).
For the PAL task, n = 13 Ctrl[Male] and n = 16 Atrx-cKO[Male] mice. For the VPD task, n = 14 Ctrl[Male] and n = 15 Atrx-cKO[Male] mice. Statistics by 2-way repeated-measures ANOVA with Sidak's multiple comparisons test were applied in all of the panels, except for (G), in which Student's t test was applied. Asterisks indicate p < 0.05. See also Videos S1 and S2.

nose pokes during the baseline tests or after reversal compared to control mice, indicating that vision is intact in the *Atrx*-cKO[Male] mice (F = 1.39, p = 0.25; Figure 4H). They did, however, require an increased number of correction trials, suggesting that their cognitive flexibility may be marginally impaired compared to controls (F = 11.84, p = 0.002; Figure 4I). The results of these tests reinforce the notion that *Atrx*-cKO[Male] mice have significant deficits in learning and memory.

Transcriptional Changes Caused by Deletion of Atrx in Hippocampal Neurons

To identify the molecular mechanisms leading to spatial memory impairment, we performed RNA sequencing of hippocampi obtained from three pairs of Ctrl[Male]/*Atrx*-cKO[Male] and Ctrl[Fem]/*Atrx*-cKO[Fem] mice. Principal-component analysis of detected transcripts (n = 126,928 transcripts) confirms the difference between male and female mice (Figure S6A). We analyzed the effects of ATRX loss for each sex independently (DESeq2, false discovery rate [FDR] < 0.1), yielding 1,024 differentially expressed transcripts in Atrx-cKO[Male] versus Ctrl[Male] mice and 2,463 differential transcripts between Atrx-cKO[Fem] and Ctrl[Fem] mice (Figure 5A; Tables S1 and S2). Among the 491 transcripts downregulated in *Atrx*-cKO[Male] mice, 42 were also downregulated in *Atrx*-cKO[Fem] mice (Figure S6B). Among the 533 transcripts upregulated in *Atrx*-cKO[Male] mice, 7 were also significantly upregulated in *Atrx*-cKO[Fem] mice (Figure S6B). We also identified 25 transcripts significantly associated with the loss of ATRX in both sexes, but with opposite directionality. Predictably, many transcripts are differentially expressed according to sex (Figure S6B). Among the 10,476 transcripts associated with sex in both KO and control mice, 5,157 were upregulated and

5,224 were downregulated in male compared with female mice, respectively (Figure S6B).

We identified 1,054 transcripts differentially expressed with genotype as a function of sex (sex*genotype interaction, FDR < 0.05) (Table S3). Functional classification revealed that these transcripts are enriched in biological processes such as "synapse organization," "cell projection organization," and "neurogenesis" (Figure 5B). We list the 41 transcripts corresponding to the top category "synpase organization" GO: 0050808; (Figure 5C), including many well-known synaptic molecules such as SH3 and multiple ankyrin repeat domains protein 2 (Shank2). Thus, comparative transcript profiling of the hippocampus identifies many synaptic transcripts that are altered as a function of sex and genotype, implicating them in either causing deficits in the Atrx-cKO[Male] mice or perhaps protecting Atrx-cKO[Fem] mice but not Atrx-cKO[Male] from such deficits.

The transcripts exhibiting sex*genotype interaction were further categorized into 4 clusters with similar patterns of expression across samples (Figure 5D). There are 292 transcripts that are upregulated in Atrx-cKO[Fem] versus Ctrl[Fem] but downregulated in Atrx-cKO[Male] versus Ctrl[Male] hippocampus (cluster 1), 134 transcripts upregulated in Atrx-cKO[Male] versus Ctrl[Male] but largely unchanged in Atrx-cKO[Fem] versus Ctrl[Fem] (cluster 2), 262 transcripts downregulated in Atrx-cKO[Fem] versus Ctrl[Fem] but upregulated in Atrx-cKO[Male] versus Ctrl[Male] hippocampus (cluster 3), and 366 transcripts that are downregulated in Atrx-cKO[Fem] versus Ctrl[Fem] but not altered in Atrx-cKO[Male] versus Ctrl[Male] (cluster 4). Heatmaps of the transcripts identified in each cluster are shown in Figure 5E and cluster annotations are listed in Table S3.
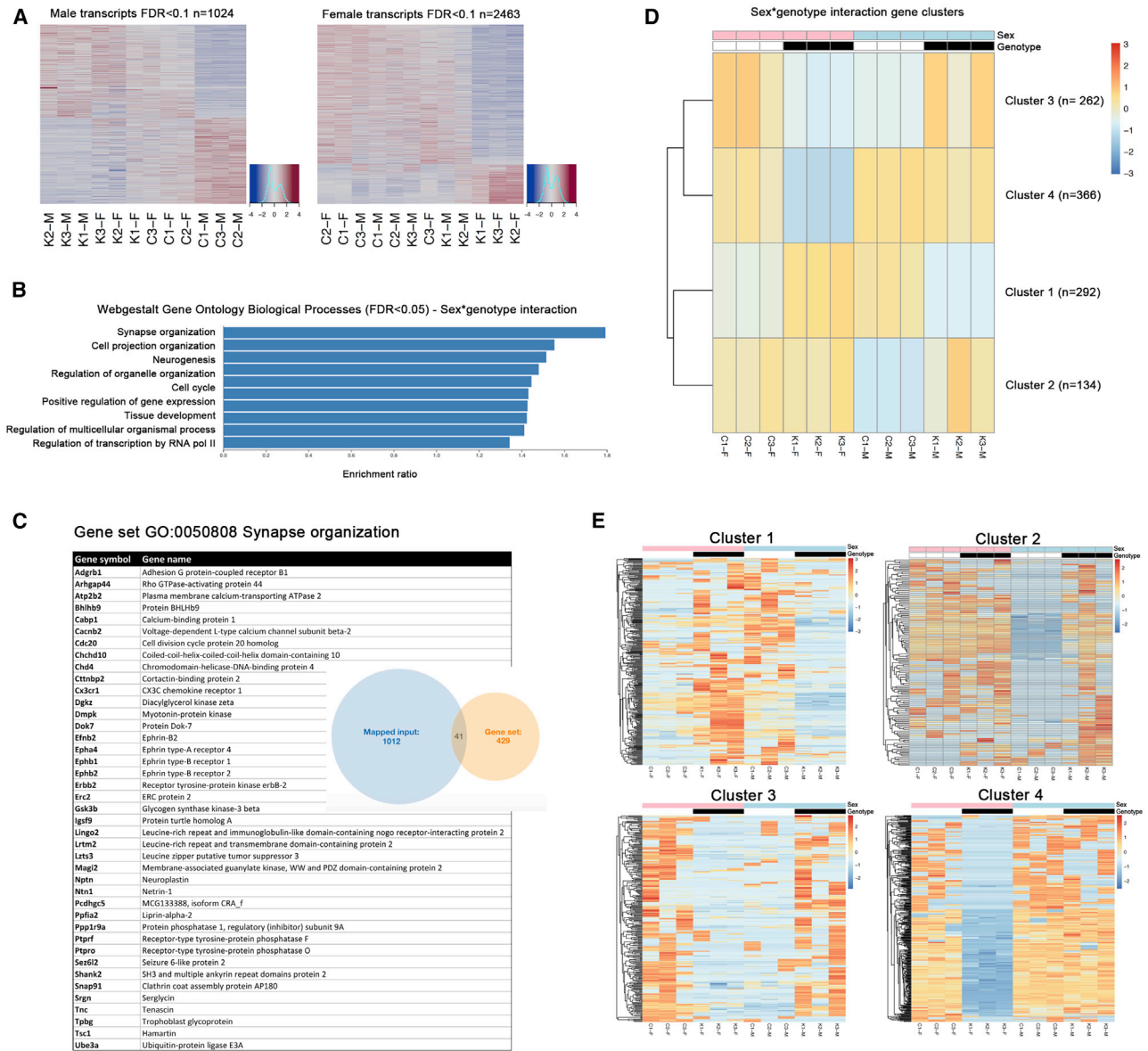
Figure 5. Identification of Hippocampal Transcripts Differentially Expressed According to Sex and Genotype

(A) RNA sequencing analysis was performed on Ctrl^{Male}(C-M), Atrx-cKO^{Male}(K-M), Ctrl^{Fem}(C-F), and Atrx-cKO^{Fem}(K-F) hippocampi (n = 3 each genotype), and an expression heatmap of the transcripts altered upon loss of ATRX was generated in male (left) and in female (right) mice, respectively (FDR < 0.1).

(B) Functional classification of sexually dimorphic transcripts identified in the hippocampus (biological processes, FDR < 0.05).

(C) List of genes included in the top category "synapse organization" identified by pathway analysis.

(D) Transcripts differentially expressed as a function of sex and genotype clustered into 4 categories. The number of genes in each cluster is indicated at right.

(E) Summary heatmaps of transcripts in clusters 1–4 identified in (D).

See also Figure S6 and Tables S1, S2, and S3.

Regulation of miR-137 and Its Target Genes by ATRX

Considering the presynaptic defects identified by EM and the transcriptional profiling results, we next considered the potential contribution of microRNAs (miRNAs) downstream of ATRX that may regulate synaptic pathways. Certain miRNAs are enriched within presynaptic terminals and have been implicated in neurotransmitter release by controlling the expression of SNARE and other synaptic vesicle proteins (Ryan et al., 2015). These miRNAs

include miR-485, miR-34a, miR-137, and miR-27b. Using a candidate approach, we set out to directly test whether these miRNAs could be regulated by ATRX, with differential effects in male and female cKO hippocampi. qRT-PCR analysis showed similar expressions of miR-485, miR-34a, and miR-27b in male or female cKO hippocampi compared to controls. Conversely, we observed a striking and significant sex-specific effect of ATRX loss on the expression of miR-137 (Figure 6A). The latter
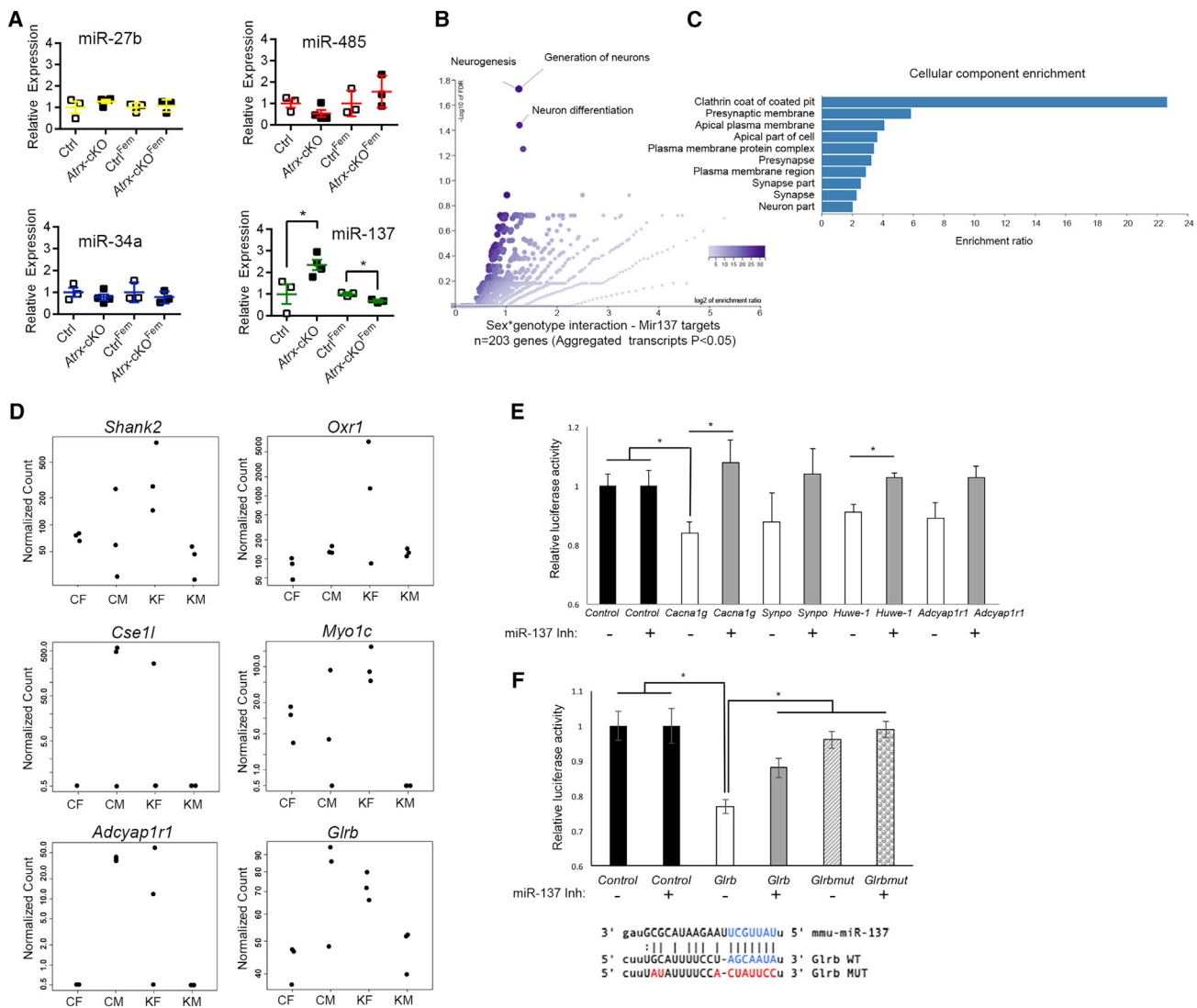
Figure 6. Sexually Dimorphic Effects of *Atrx* Neuronal Deletion on the Expression of miR-137 and Some of Its Target Genes

(A) qRT-PCR analysis of miR-485, miR-34a, miR-485, and miR-137 in Ctrl[Male], Atrx-cKO[Male], Ctrl[Fem], and Atrx-cKO[Fem] hippocampi normalized to a control miRNA (miR-191).

(B and C) Top GO enrichment categories for biological processes (B) and cellular components (C) obtained from the list of predicted miR-137 targets differentially expressed according to sex and genotype.

(D) Examples of transcripts that are differentially expressed according to sex and genotype and that were previously validated (*Shank2*, *Oxr1*, *Cse1l*, *Myo1C*) or that are predicted (*Adcyap1r1*, *Glrb*) miR-137 targets.

(E) Candidate miR-137 target genes were tested by a dual luciferase reporter assay with empty vector (Control) or the wild-type miR-137 gene target sequence in the presence or absence of a miR-137 inhibitor (n = 3).

(F) The predicted miR-137 binding sites of the *GlrB* 3′ UTR sequence can mediate suppression of the luciferase gene, while a mutated sequence or the presence of a miR-137 inhibitor alleviates this repression (p < 0.05, Student's t test). Sequences of the *Glrb WT* and *Glrb MUT* are shown below the graph.

The data are displayed as means ± SEMs, and asterisks indicate p < 0.05. See also Figure S7 and Table S3.

is upregulated in the Atrx-cKO[Male] compared to Ctrl[Male] hippocampi but significantly reduced in Atrx-cKO[Fem] compared to Ctrl[Fem] (Figure 6A). We curated 3,512 genes that are predicted targets of miR-137 and investigated how corresponding transcripts are expressed across our 4 groups (Ctrl[Male]/*Atrx*-cKO[Male] and Ctrl[Fem]/*Atrx*-cKO[Fem]). We identified 203 miR-137 targets that were differentially associated with genotype according to sex (sex*genotype interaction; Lancaster p < 0.05, from aggre-

gated transcripts) (Yi et al., 2018; Table S3). GO analysis of this sub-list identified enrichment for biological processes such as "neurogenesis," "generation of neurons," and "neuron differentiation" (Figure 6B). Enrichment for cellular components identified "clathrin coat of coated pit," "presynaptic membrane," "apical plasma membrane," and "presynapse" as some of the top categories (Figure 6C), corresponding to the presynaptic defects we identified by EM. Several of the gene targets showing
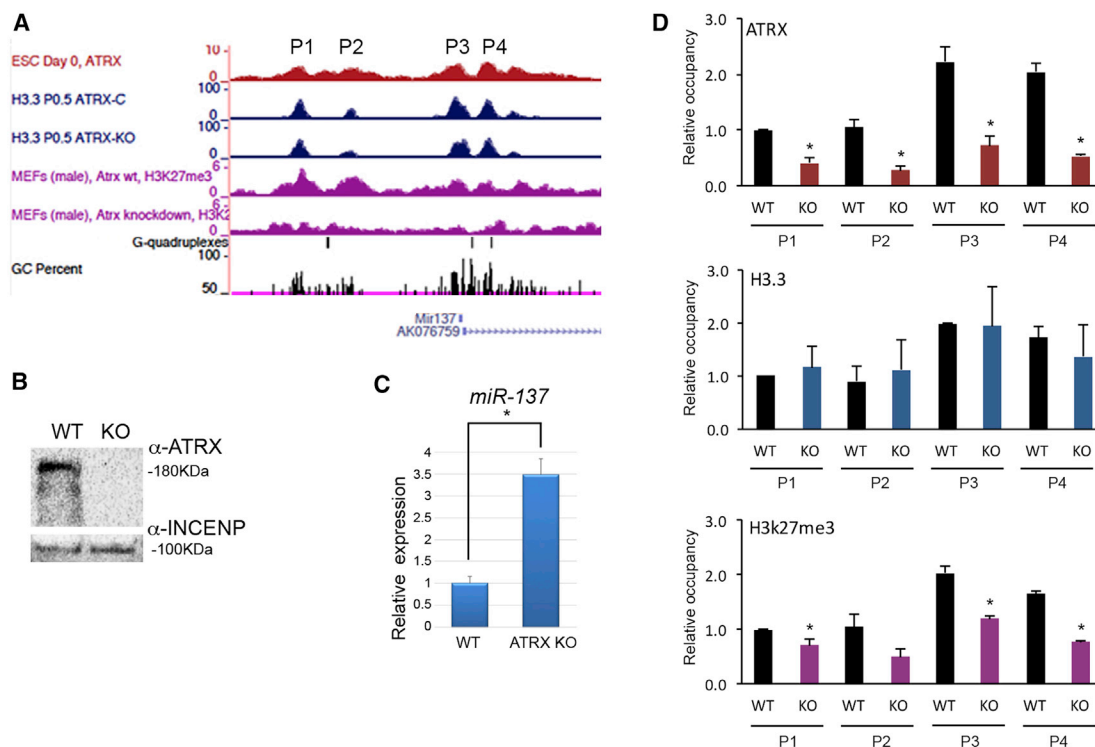
Figure 7. ATRX Occupies the miR-137 Gene Locus and Regulates H3K27me3 Occupancy

(A) Chromatin immunoprecipitation sequencing (ChIP-seq) of ATRX in embryonic stem cells (ESCs) (Sarma et al., 2014), H3.3 in control and ATRX KO newborn forebrain (Levy et al., 2015), and H3K27me3 in mouse embryonic fibroblasts (MEFs) (Sarma et al., 2014) at the miR-137 genomic locus. Predicted G-quadruplex-forming sequences and guanine-cytosine (GC) percent are shown below the ChIP-seq tracks. P1–P4 refers to 4 major peaks of ATRX occupancy.

(B) Western blot validating CRISPR-Cas9-mediated KO of ATRX in Neuro2A cells. INCENP levels were used to normalize ATRX expression.

(C) Increased expression of miR-137 in ATRX KO compared to wild-type Neuro2A cells (p < 0.05, Student's t test).

(D) ChIP-qPCR of ATRX, H3.3, and H3K27me3 in Neuro2A cells shows occupancy at the P1, P2, P3, and P4 sites of the miR-137 locus, as depicted in (A). The loss of ATRX does not affect H3.3 occupancy, but it does lead to decreased H3K27me3 at the miR-137 locus (n = 3, asterisks indicate p < 0.05, Student's t test).

sex*genotype interaction, such as *Shank2*, *Oxr1*, *Cse1l*, and *Myo1C* have previously been validated as miR-137 targets (de Sena Cortabitarte et al., 2018; Du et al., 2016; Jiang et al., 2019; Li et al., 2013; Figure 6D). Other differentially expressed genes, including *Cacna1g*, *Glrb*, *Synpo*, *Huwe-1*, and *Adcyap1r1* have not yet been experimentally validated (Figures 6D and S7). We introduced the putative miR-137 target sequence for these genes at the 3′ UTR of a luciferase reporter construct. Neuro2A cells expressing lentiviral miR-137 were transfected with the luciferase constructs, and luciferase activity was measured 48 h later. The results show a decrease in luciferase activity for each putative miR-137 target compared to vector alone, reaching statistical significance for *Cacna1g* and *Glrb* (Figure 6E). A miR-137 inhibitor significantly increased luciferase expression for *Cacna1g*, *Huwe-1*, and *Glrb* constructs. We also show that a mutated version of the *Glrb* target sequence lacked the ability to suppress luciferase activity when compared to the wild-type version (Figure 6F). The evidence suggests that miR-137 is differentially expressed upon the loss of ATRX in male and female mice, as well as some of its gene targets.

Analysis of sequence data previously published by us and others (Levy et al., 2015; Sarma et al., 2014) shows that the miR-137 genomic locus has four major ATRX binding sites in mouse embryonic stem cells (annotated P1–P4; Figure 7A). These sites correspond to peaks of histone H3.3 and of the suppressive histone mark H3K27me3 (Figure 7A). Loss of ATRX does not interfere with H3.3 occupancy at these sites, but there is a dramatic decrease in H3K27me3 in the ATRX KO mouse embryonic fibroblasts (Figure 7A). We generated Neuro2A ATRX KO cells (male neuroblastoma cells) using the CRISPR-Cas targeting approach (Figure 7B) and show that they exhibit a ~3.5-fold increase in miR-137 expression compared to control cells (Figure 7C); this provides an adequate model of our *in vivo* observations in the male hippocampus. We performed chromatin immunoprecipitation for ATRX, H3.3, and H3K27me3 in Neuro2A control and ATRX KO cells. qPCR of P1, P2, P3, and P4 sites show binding of ATRX at all 4 sites, similar to our observation in embryonic stem cells. H3.3 is also enriched at all sites, but it is not significantly changed in the ATRX KO cells. Conversely, H3K27me3 occupancy is significantly decreased at P1, P3, and P4 sites in ATRX null Neuro2A cells compared to controls (Figure 7D). Based on these results, we conclude that ATRX directly regulates miR-137 expression and that the observed increase of miR-137 in ATRX null cells may be caused, at least in part, by decreased trimethylation at H3 lysine 27.

DISCUSSION

This study presents evidence that ATRX is required in a sex-specific manner in excitatory forebrain neurons for normal spatial learning and memory. Loss of ATRX in the *Atrx*-cKO[Male] mice resulted in various hippocampal-dependent memory impairments, including contextual fear memory, and spatial learning and memory in the Morris water maze and paired-associate touchscreen tasks. The results from the touchscreen task are especially valuable, considering their translational potential (Bussey et al., 2012), and that comparable results to humans are achieved using mouse models of cognitive impairment (Nithiananantharajah et al., 2013, 2015).

Examination of the ATRX mutant brain by MRI identified hippocampal morphological defects that may be related to the memory impairments. We originally hypothesized that the increased volume of the CA1 SR and SLM may be due to increased branching of pyramidal neurons, particularly the apical dendrites that project to this region. However, analysis of Golgi-stained CA1 neurons failed to identify abnormalities in dendritic branching that would explain the MRI data. Astrocyte and microglia infiltration have been linked with defects in learning and memory in various mouse models (Bian et al., 2012; McGill et al., 2018; Tanaka et al., 2006). However, after examination of these cell types by immunofluorescence staining, we detected no change in either astrocyte or microglia cell number. The reason for the volume increase thus remains undetermined, but may be caused by an increased volume of the perineuronal net (changes to the extracellular matrix), which has been shown to help regulate learning and memory (Bukalo et al., 2001; Hylin et al., 2013). An alternative explanation is that volumetric measurements are normal in these areas, but decreased elsewhere in the hippocampus.

There are two hippocampal pathways implicated in spatial learning and memory, the Schaffer collateral pathway and the temporoammonic pathway. The Schaffer collateral pathway involves the CA3 axons projecting to the CA1 medial apical dendrites (Vago and Kesner, 2008), whereas the temporoammonic pathway initiates in layer III of the entorhinal cortex and projects to the CA1 middle apical dendritic layer (Nguyen and Kandel, 1996). We recently reported impaired hippocampal apical dendritic CA1 long-term potentiation (LTP), which could account for the spatial memory deficits reported here (Gugustea et al., 2020). The temporoammonic pathway, thought to be critical for long-term spatial memory recall or consolidation (Brun et al., 2008; Remondes and Schuman, 2004), showed significantly reduced LTP in anesthetized Atrx-cKO[Male] mice compared to control mice (Gugustea et al., 2020).

Unexpectedly, *Atrx*-cKO[Fem] mice did not show impairments in learning and memory paradigms. In humans, females harboring *ATRX* mutations are largely protected from the disease as a result of the skewing of X-inactivation (Gibbons et al., 1992); however, this is not the case here, since the mice were homozygous for the "floxed" allele and we confirmed by immunofluorescence staining that ATRX is indeed absent from hippocampal excitatory neurons. Sexual dimorphism has been reported in other mouse models with mutations in chromatin remodeling proteins, including CHD8 and MeCP2, in which females are un-

affected by the loss of the protein of interest or are affected differently (Jung et al., 2018; Kim et al., 2016; Kurian et al., 2008). Developmental neurological diseases such as autism spectrum disorders tend to preferentially affect males, possibly due to combinatorial contributions of hormonal and genetic factors in a phenomenon known as the female protective effect (Fombonne, 2009; Jacquemont et al., 2014; Voineagu et al., 2011), and this has repeatedly been demonstrated in mouse models (Hu et al., 2015; Sato et al., 2012; Tsutiya et al., 2017). The presence of estrogen and estrogen receptor in the female brain has been shown to be neuroprotective and lead to enhanced Schaffer collateral LTP (Wang et al., 2018). In addition, certain X-linked genes involved in chromatin regulation (e.g., *Utx*, a histone demethylase) are able to escape X-inactivation and thus are expressed 2-fold in females compared to males (Xu et al., 2008). These mechanisms could lead to protective effects in the *Atrx*-cKO[Fem] mice, causing sexually dimorphic defects in learning and memory. We previously reported impairment of spatial learning and memory in a female mouse model with mosaic expression of ATRX in all types of cells of the central nervous system (Tamming et al., 2017). This suggests the intriguing possibility that female-specific protective factors originate from cell types other than the excitatory neurons targeted in the present study. Female-specific glial factors, for example, may provide important protection against the loss of ATRX in neurons.

Another mechanism that could explain the divergent behaviors between male and female mice is the opposite effect of ATRX loss on miR-137 expression. miRNAs are critical for the regulation of transcriptional programs in the brain. At the molecular level, miRNAs can target hundreds to thousands of genes, thereby altering the expression of proteins at the presynaptic terminal, the postsynaptic membrane, or both. The TEM and RNA sequencing data obtained in the present study identified impaired presynaptic vesicular function, with a decreased number of docked and total vesicles. miR-137 overexpression has previously been linked to impaired hippocampal-dependent learning and memory in the Morris water maze and contextual fear conditioning task, similar to the *Atrx*-cKO mice (Siegert et al., 2015). In addition, miR-137 overexpression results in altered vesicular trafficking and reduced LTP *in vivo* and a reduction in the number of docked and total vesicles *in vitro* (He et al., 2018; Siegert et al., 2015), again paralleling our findings in *Atrx*-cKO[Male] mice. miR-137 is also known to regulate the expression of genes involved in postsynaptic function, including *N*-methyl-D-aspartate (NMDA) and AMPA receptor synthesis (Olde Loohuis et al., 2015; Zhao et al., 2013) and multiple targets in the phosphatidylinositol 3-kinase-Akt-mammalian target of rapamycin (PI3K-Akt-mTOR) pathway (Thomas et al., 2017). Therefore, the increased expression of miR-137 could explain the presynaptic defects seen in *Atrx*-cKO male mice and may have other effects within the PSD and downstream signaling that should be examined in more detail in the future. Several sexually dimorphic miR-137 target genes were identified that may contribute to the memory deficits in males or their absence in females. SHANK2 acts as a scaffolding protein within the PSD of excitatory synapses, connecting glutamate receptors to the actin-based cytoskeleton (Sheng and Kim, 2000). Oxidation resistance 1 (OXR1) has been implicated in limiting oxidative stress-mediated DNA damage (Oliver et al., 2011). Very recently, *Oxr1*

null mutations were identified in an autosomal-recessive neurological disorder associated with severe global developmental delay, intellectual disability, language delay, cerebellar atrophy, and seizures (Jiang et al., 2019; Zhou et al., 2019). Moreover, the inhibition of miR-137 or the upregulation of its target gene *Oxr1* ameliorated oxidative stress injury in a Parkinson disease model (Jiang et al., 2019). Glycine receptor B (*GLRB*) mutations cause congenital hyperekplexia, a neuromotor disorder characterized by stiffness and easily provoked startle responses, and many cases also have developmental cognitive delay (Thomas et al., 2013). The HECT, UBA, and WWE domain containing 1 (*HUWE1*) gene encodes a E3 ubiquitin ligase that targets its substrates for proteasomal degradation via poly-ubiquitination. *HUWE1* mutations are associated with intellectual disability (Moortgat et al., 2018). A *HUWE1* mutation was identified in an affected male from the original family reported by Juberg and Marsidi that was originally erroneously attributed to an *ATRX* mutation (Friez et al., 2016), highlighting the similarity of clinical phenotypes incurred by *ATRX* and *HUWE1* mutations. It is possible that the effects of ATRX neuronal deletion on memory derive from the misregulation of many different miR-137 targets in the hippocampus.

We determined that ATRX binds four distinct sites at the miR-137 gene locus that are also occupied by the histone variant H3.3. Although ATRX and the DAXX histone chaperone have been implicated in H3.3 deposition at some genomic sites, we observed no change in H3.3 levels at miR-137 in ATRX null Neuro2A cells, perhaps due to compensatory mechanisms. Conversely, we detected a significant decrease in the suppressive histone mark H3K27me3, offering a potential mechanism for miR-137 de-repression in ATRX null cells.

Unfortunately, the coronavirus disease 2019 pandemic limited our ability to complete a number of experiments that would have further supported our conclusions. In particular, additional analyses of *Atrx*-cKO^Fem mice would have helped to further strengthen the connection between the molecular findings and the sexually dimorphic phenotypes. In addition, modulation of the miR-137 levels in the hippocampus would provide more direct evidence of its association with the observed synaptic defects and memory deficits. Nevertheless, our study presents strong evidence that ATRX is required in forebrain excitatory neurons for spatial learning and long-term memory and the regulation of genes required for efficient synaptic transmission.

STAR★METHODS

Detailed methods are provided in the online version of this paper and include the following:

SUPPLEMENTAL INFORMATION

Supplemental Information can be found online at https://doi.org/10.1016/j.celrep.2020.107838.

AUTHOR CONTRIBUTIONS

Conceptualization, R.J.T. and N.G.B.; Methodology, R.J.T., V.D., J.E., and L.R.Q.; Investigation, R.J.T., S.S., Y.J., and L.L.; Formal Analysis, V.D., J.E., and L.R.Q.; Software, V.D.; Writing – Original Draft, R.J.T. and N.G.B.; Writing – Review & Editing, R.J.T. and N.G.B. Visualization, R.J.T., V.D., and N.G.B.; Resources, V.D., J.P.L., and N.G.B.; Supervision, J.P.L. and N.G.B.; Funding Acquisition, J.L. and N.G.B.

DECLARATION OF INTERESTS

The authors declare no competing interests.

Cell Reports
Article

REFERENCES

Avants, B.B., Tustison, N.J., Wu, J., Cook, P.A., and Gee, J.C. (2011). An open source multivariate framework for n-tissue segmentation with evaluation on public data. Neuroinformatics *9*, 381–400.

Benjamini, Y., and Hochberg, Y. (1995). Controlling the false discovery rate: a practical and powerful approach to multiple testing. J. R. Stat. Soc. B *57*, 289–300.

Bérubé, N.G., Mangelsdorf, M., Jagla, M., Vanderluit, J., Garrick, D., Gibbons, R.J., Higgs, D.R., Slack, R.S., and Picketts, D.J. (2005). The chromatin-remodeling protein ATRX is critical for neuronal survival during corticogenesis. J. Clin. Invest. *115*, 258–267.

Bian, Y., Pan, Z., Hou, Z., Huang, C., Li, W., and Zhao, B. (2012). Learning, memory, and glial cell changes following recovery from chronic unpredictable stress. Brain Res. Bull. *88*, 471–476.

Bisht, K., El Hajj, H., Savage, J.C., Sánchez, M.G., and Tremblay, M.E. (2016). Correlative Light and Electron Microscopy to Study Microglial Interactions with β-Amyloid Plaques. J. Vis. Exp. (*112*), 54060.

Brun, V.H., Leutgeb, S., Wu, H.Q., Schwarcz, R., Witter, M.P., Moser, E.I., and Moser, M.B. (2008). Impaired spatial representation in CA1 after lesion of direct input from entorhinal cortex. Neuron *57*, 290–302.

Bukalo, O., Schachner, M., and Dityatev, A. (2001). Modification of extracellular matrix by enzymatic removal of chondroitin sulfate and by lack of tenascin-R differentially affects several forms of synaptic plasticity in the hippocampus. Neuroscience *104*, 359–369.

Bussey, T.J., Padain, T.L., Skillings, E.A., Winters, B.D., Morton, A.J., and Saksida, L.M. (2008). The touchscreen cognitive testing method for rodents: how to get the best out of your rat. Learn. Mem. *15*, 516–523.

Bussey, T.J., Holmes, A., Lyon, L., Mar, A.C., McAllister, K.A., Nithianantharajah, J., Oomen, C.A., and Saksida, L.M. (2012). New translational assays for preclinical modelling of cognition in schizophrenia: the touchscreen testing method for mice and rats. Neuropharmacology *62*, 1191–1203.

Collins, D.L., Neelin, P., Peters, T.M., and Evans, A.C. (1994). Automatic 3D intersubject registration of MR volumetric data in standardized Talairach space. J. Comput. Assist. Tomogr. *18*, 192–205.

de Castro, B.M., Pereira, G.S., Magalhães, V., Rossato, J.I., De Jaeger, X., Martins-Silva, C., Leles, B., Lima, P., Gomez, M.V., Gainetdinov, R.R., et al. (2009). Reduced expression of the vesicular acetylcholine transporter causes learning deficits in mice. Genes Brain Behav. *8*, 23–35.

de Guzman, A.E., Wong, M.D., Gleave, J.A., and Nieman, B.J. (2016). Variations in post-perfusion immersion fixation and storage alter MRI measurements of mouse brain morphometry. Neuroimage *142*, 687–695.

de Sena Cortabitarte, A., Berkel, S., Cristian, F.B., Fischer, C., and Rappold, G.A. (2018). A direct regulatory link between microRNA-137 and SHANK2: implications for neuropsychiatric disorders. J. Neurodev. Disord. *10*, 15.

Delotterie, D.F., Mathis, C., Cassel, J.C., Rosenbrock, H., Dorner-Ciossek, C., and Marti, A. (2015). Touchscreen tasks in mice to demonstrate differences between hippocampal and striatal functions. Neurobiol. Learn. Mem. *120*, 16–27.

Dorr, A.E., Lerch, J.P., Spring, S., Kabani, N., and Henkelman, R.M. (2008). High resolution three-dimensional brain atlas using an average magnetic resonance image of 40 adult C57Bl/6J mice. Neuroimage *42*, 60–69.

Du, Y., Chen, Y., Wang, F., and Gu, L. (2016). miR-137 plays tumor suppressor roles in gastric cancer cell lines by targeting KLF12 and MYO1C. Tumour Biol. *37*, 13557–13569.

Eustermann, S., Yang, J.C., Law, M.J., Amos, R., Chapman, L.M., Jelinska, C., Garrick, D., Clynes, D., Gibbons, R.J., Rhodes, D., et al. (2011). Combinatorial readout of histone H3 modifications specifies localization of ATRX to heterochromatin. Nat. Struct. Mol. Biol. *18*, 777–782.

Ferreira, T.A., Blackman, A.V., Oyrer, J., Jayabal, S., Chung, A.J., Watt, A.J., Sjöström, P.J., and van Meyel, D.J. (2014). Neuronal morphometry directly from bitmap images. Nat. Methods *11*, 982–984.

Fombonne, E. (2009). Epidemiology of pervasive developmental disorders. Pediatr. Res. *65*, 591–598.

Friez, M.J., Brooks, S.S., Stevenson, R.E., Field, M., Basehore, M.J., Adès, L.C., Sebold, C., McGee, S., Saxon, S., Skinner, C., et al. (2016). HUWE1 mutations in Juberg-Marsidi and Brooks syndromes: the results of an X-chromosome exome sequencing study. BMJ Open *6*, e009537.

Garrick, D., Sharpe, J.A., Arkell, R., Dobbie, L., Smith, A.J., Wood, W.G., Higgs, D.R., and Gibbons, R.J. (2006). Loss of Atrx affects trophoblast development and the pattern of X-inactivation in extraembryonic tissues. PLOS Genet. *2*, e58.

Genovese, C.R., Lazar, N.A., and Nichols, T. (2002). Thresholding of statistical maps in functional neuroimaging using the false discovery rate. Neuroimage *15*, 870–878.

Gibbons, R.J., Suthers, G.K., Wilkie, A.O., Buckle, V.J., and Higgs, D.R. (1992). X-linked alpha-thalassemia/mental retardation (ATR-X) syndrome: localization to Xq12-q21.31 by X inactivation and linkage analysis. Am. J. Hum. Genet. *51*, 1136–1149.

Gibbons, R.J., Picketts, D.J., Villard, L., and Higgs, D.R. (1995). Mutations in a putative global transcriptional regulator cause X-linked mental retardation with alpha-thalassemia (ATR-X syndrome). Cell *80*, 837–845.

Gibbons, R.J., Bachoo, S., Picketts, D.J., Aftimos, S., Asenbauer, B., Bergoffen, J., Berry, S.A., Dahl, N., Fryer, A., Keppler, K., et al. (1997). Mutations in transcriptional regulator ATRX establish the functional significance of a PHD-like domain. Nat. Genet. *17*, 146–148.

Gibbons, R.J., Wada, T., Fisher, C.A., Malik, N., Mitson, M.J., Steensma, D.P., Fryer, A., Goudie, D.R., Krantz, I.D., and Traeger-Synodinos, J. (2008). Mutations in the chromatin-associated protein ATRX. Hum. Mutat. *29*, 796–802.

Goldberg, A.D., Banaszynski, L.A., Noh, K.M., Lewis, P.W., Elsaesser, S.J., Stadler, S., Dewell, S., Law, M., Guo, X., Li, X., et al. (2010). Distinct factors control histone variant H3.3 localization at specific genomic regions. Cell *140*, 678–691.

Grozeva, D., Carss, K., Spasic-Boskovic, O., Tejada, M.I., Gecz, J., Shaw, M., Corbett, M., Haan, E., Thompson, E., Friend, K., et al.; Italian X-linked Mental Retardation Project; UK10K Consortium; GOLD Consortium (2015). Targeted Next-Generation Sequencing Analysis of 1,000 Individuals with Intellectual Disability. Hum. Mutat. *36*, 1197–1204.

Gugustea, R., Tamming, R.J., Martin-Kenny, N., Bérubé, N.G., and Leung, L.S. (2020). Inactivation of ATRX in forebrain excitatory neurons affects hippocampal synaptic plasticity. Hippocampus *30*, 565–581.

Harris, K.M., Jensen, F.E., and Tsao, B. (1992). Three-dimensional structure of dendritic spines and synapses in rat hippocampus (CA1) at postnatal day 15 and adult ages: implications for the maturation of synaptic physiology and long-term potentiation. J. Neurosci. *12*, 2685–2705.

He, E., Lozano, M.A.G., Stringer, S., Watanabe, K., Sakamoto, K., den Oudsten, F., Koopmans, F., Giambverardino, S.N., Hammerschlag, A., Cornelisse, L.N., et al. (2018). MIR137 schizophrenia-associated locus controls synaptic function by regulating synaptogenesis, synapse maturation and synaptic transmission. Hum. Mol. Genet. *27*, 1879–1891.

Hu, V.W., Sarachana, T., Sherrard, R.M., and Kocher, K.M. (2015). Investigation of sex differences in the expression of RORA and its transcriptional targets in the brain as a potential contributor to the sex bias in autism. Mol. Autism *6*, 7.

Hylin, M.J., Orsi, S.A., Moore, A.N., and Dash, P.K. (2013). Disruption of the perineuronal net in the hippocampus or medial prefrontal cortex impairs fear conditioning. Learn. Mem. *20*, 267–273.

Ignatiadis, N., Klaus, B., Zaugg, J.B., and Huber, W. (2016). Data-driven hypothesis weighting increases detection power in genome-scale multiple testing. Nat. Methods *13*, 577–580.

Jacquemont, S., Coe, B.P., Hersch, M., Duyzend, M.H., Krumm, N., Bergmann, S., Beckmann, J.S., Rosenfeld, J.A., and Eichler, E.E. (2014). A higher mutational burden in females supports a "female protective model" in neurodevelopmental disorders. Am. J. Hum. Genet. *94*, 415–425.

Jiang, Y., Liu, J., Chen, L., Jin, Y., Zhang, G., Lin, Z., Du, S., Fu, Z., Chen, T., Qin, Y., and Sun, X. (2019). Serum secreted miR-137-containing exosomes

affects oxidative stress of neurons by regulating OXR1 in Parkinson's disease. Brain Res. *1722*, 146331.

Jung, H., Park, H., Choi, Y., Kang, H., Lee, E., Kweon, H., Roh, J.D., Ellegood, J., Choi, W., Kang, J., et al. (2018). Sexually dimorphic behavior, neuronal activity, and gene expression in Chd8-mutant mice. Nat. Neurosci. *21*, 1218–1228.

Kernohan, K.D., Jiang, Y., Tremblay, D.C., Bonvissuto, A.C., Eubanks, J.H., Mann, M.R., and Bérubé, N.G. (2010). ATRX partners with cohesin and MeCP2 and contributes to developmental silencing of imprinted genes in the brain. Dev. Cell *18*, 191–202.

Kim, C.H., Heath, C.J., Kent, B.A., Bussey, T.J., and Saksida, L.M. (2015). The role of the dorsal hippocampus in two versions of the touchscreen automated paired associates learning (PAL) task for mice. Psychopharmacology (Berl.) *232*, 3899–3910.

Kim, K.C., Choi, C.S., Kim, J.W., Han, S.H., Cheong, J.H., Ryu, J.H., and Shin, C.Y. (2016). MeCP2 Modulates Sex Differences in the Postsynaptic Development of the Valproate Animal Model of Autism. Mol. Neurobiol. *53*, 40–56.

Kolde, R. (2012). "Pheatmap: pretty heatmaps.". R package version *61*, 617.

Kurian, J.R., Bychowski, M.E., Forbes-Lorman, R.M., Auger, C.J., and Auger, A.P. (2008). Mecp2 organizes juvenile social behavior in a sex-specific manner. J. Neurosci. *28*, 7137–7142.

Law, M.J., Lower, K.M., Voon, H.P., Hughes, J.R., Garrick, D., Viprakasit, V., Mitson, M., De Gobbi, M., Marra, M., Morris, A., et al. (2010). ATR-X syndrome protein targets tandem repeats and influences allele-specific expression in a size-dependent manner. Cell *143*, 367–378.

Lerch, J.P., Carroll, J.B., Dorr, A., Spring, S., Evans, A.C., Hayden, M.R., Sled, J.G., and Henkelman, R.M. (2008). Cortical thickness measured from MRI in the YAC128 mouse model of Huntington's disease. Neuroimage *41*, 243–251.

Levy, M.A., Kernohan, K.D., Jiang, Y., and Bérubé, N.G. (2015). ATRX promotes gene expression by facilitating transcriptional elongation through guanine-rich coding regions. Hum. Mol. Genet. *24*, 1824–1835.

Lewis, P.W., Elsaesser, S.J., Noh, K.M., Stadler, S.C., and Allis, C.D. (2010). Daxx is an H3.3-specific histone chaperone and cooperates with ATRX in replication-independent chromatin assembly at telomeres. Proc. Natl. Acad. Sci. USA *107*, 14075–14080.

Li, H., Handsaker, B., Wysoker, A., Fennell, T., Ruan, J., Homer, N., Marth, G., Abecasis, G., and Durbin, R.; 1000 Genome Project Data Processing Subgroup (2009). The Sequence Alignment/Map format and SAMtools. Bioinformatics *25*, 2078–2079. https://doi.org/10.1093/bioinformatics/btp352.

Li, K.K., Yang, L., Pang, J.C., Chan, A.K., Zhou, L., Mao, Y., Wang, Y., Lau, K.M., Poon, W.S., Shi, Z., and Ng, H.K. (2013). MIR-137 suppresses growth and invasion, is downregulated in oligodendroglial tumors and targets CSE1L. Brain Pathol. *23*, 426–439.

Longair, M.H., Baker, D.A., and Armstrong, J.D. (2011). Simple Neurite Tracer: open source software for reconstruction, visualization and analysis of neuronal processes. Bioinformatics *27*, 2453–2454.

Love, M.I., Huber, W., and Anders, S. (2014). Moderated estimation of fold change and dispersion for RNA-seq data with DESeq2. Genome Biol. *15*, 550.

Martin, M. (2011). Cutadapt removes adapter sequences from high-throughput sequencing reads. EMBnet.journal *17*, 10–12.

McGill, B.E., Barve, R.A., Maloney, S.E., Strickland, A., Rensing, N., Wang, P.L., Wong, M., Head, R., Wozniak, D.F., and Milbrandt, J. (2018). Abnormal Microglia and Enhanced Inflammation-Related Gene Transcription in Mice with Conditional Deletion of *Ctcf* in *Camk2a-Cre*-Expressing Neurons. J. Neurosci. *38*, 200–219.

Moortgat, S., Berland, S., Aukrust, I., Maystadt, I., Baker, L., Benoit, V., Caro-Llopis, A., Cooper, N.S., Debray, F.G., Faivre, L., et al. (2018). HUWE1 variants cause dominant X-linked intellectual disability: a clinical study of 21 patients. Eur. J. Hum. Genet. *26*, 64–74.

Nguyen, P.V., and Kandel, E.R. (1996). A macromolecular synthesis-dependent late phase of long-term potentiation requiring cAMP in the medial perforant pathway of rat hippocampal slices. J. Neurosci. *16*, 3189–3198.

Nieman, B.J., Flenniken, A.M., Adamson, S.L., Henkelman, R.M., and Sled, J.G. (2006). Anatomical phenotyping in the brain and skull of a mutant mouse by magnetic resonance imaging and computed tomography. Physiol. Genomics *24*, 154–162.

Nieman, B.J., van Eede, M.C., Spring, S., Dazai, J., Henkelman, R.M., and Lerch, J.P. (2018). MRI to Assess Neurological Function. Curr. Protoc. Mouse Biol. *8*, e44.

Nithianantharajah, J., Komiyama, N.H., McKechanie, A., Johnstone, M., Blackwood, D.H., St Clair, D., Emes, R.D., van de Lagemaat, L.N., Saksida, L.M., Bussey, T.J., and Grant, S.G. (2013). Synaptic scaffold evolution generated components of vertebrate cognitive complexity. Nat. Neurosci. *16*, 16–24.

Nithianantharajah, J., McKechanie, A.G., Stewart, T.J., Johnstone, M., Blackwood, D.H., St Clair, D., Grant, S.G., Bussey, T.J., and Saksida, L.M. (2015). Bridging the translational divide: identical cognitive touchscreen testing in mice and humans carrying mutations in a disease-relevant homologous gene. Sci. Rep. *5*, 14613.

Olde Loohuis, N.F., Ba, W., Stoerchel, P.H., Kos, A., Jager, A., Schratt, G., Martens, G.J., van Bokhoven, H., Nadif Kasri, N., and Aschrafi, A. (2015). MicroRNA-137 Controls AMPA-Receptor-Mediated Transmission and mGluR-Dependent LTD. Cell Rep. *11*, 1876–1884.

Oliver, P.L., Finelli, M.J., Edwards, B., Bitoun, E., Butts, D.L., Becker, E.B., Cheeseman, M.T., Davies, B., and Davies, K.E. (2011). Oxr1 is essential for protection against oxidative stress-induced neurodegeneration. PLOS Genet. *7*, e1002338.

Pertea, M., Pertea, G.M., Antonescu, C.M., Chang, T.C., Mendell, J.T., and Salzberg, S.L. (2015). StringTie enables improved reconstruction of a transcriptome from RNA-seq reads. Nat. Biotechnol. *33*, 290–295.

Picketts, D.J., Higgs, D.R., Bachoo, S., Blake, D.J., Quarrell, O.W., and Gibbons, R.J. (1996). ATRX encodes a novel member of the SNF2 family of proteins: mutations point to a common mechanism underlying the ATR-X syndrome. Hum. Mol. Genet. *5*, 1899–1907.

Qiu, L.R., Fernandes, D.J., Szulc-Lerch, K.U., Dazai, J., Nieman, B.J., Turnbull, D.H., Foster, J.A., Palmert, M.R., and Lerch, J.P. (2018). Mouse MRI shows brain areas relatively larger in males emerge before those larger in females. Nat. Commun. *9*, 2615.

Ran, F.A., Hsu, P.D., Wright, J., Agarwala, V., Scott, D.A., and Zhang, F. (2013). Genome engineering using the CRISPR-Cas9 system. Nat. Protoc. *8*, 2281–2308.

Remondes, M., and Schuman, E.M. (2004). Role for a cortical input to hippocampal area CA1 in the consolidation of a long-term memory. Nature *431*, 699–703.

Richards, K., Watson, C., Buckley, R.F., Kurniawan, N.D., Yang, Z., Keller, M.D., Beare, R., Bartlett, P.F., Egan, G.F., Galloway, G.J., et al. (2011). Segmentation of the mouse hippocampal formation in magnetic resonance images. Neuroimage *58*, 732–740.

Ryan, B., Joilin, G., and Williams, J.M. (2015). Plasticity-related microRNA and their potential contribution to the maintenance of long-term potentiation. Front. Mol. Neurosci. *8*, 4.

Sahakian, B.J., Morris, R.G., Evenden, J.L., Heald, A., Levy, R., Philpot, M., and Robbins, T.W. (1988). A comparative study of visuospatial memory and learning in Alzheimer-type dementia and Parkinson's disease. Brain *111*, 695–718.

Sarma, K., Cifuentes-Rojas, C., Ergun, A., Del Rosario, A., Jeon, Y., White, F., Sadreyev, R., and Lee, J.T. (2014). ATRX Directs Binding of PRC2 to Xist RNA and Polycomb Targets. Cell *159*, 1228.

Sato, D., Lionel, A.C., Leblond, C.S., Prasad, A., Pinto, D., Walker, S., O'Connor, I., Russell, C., Drmic, I.E., Hamdan, F.F., et al. (2012). SHANK1 Deletions in Males with Autism Spectrum Disorder. Am. J. Hum. Genet. *90*, 879–887.

Schindelin, J., Arganda-Carreras, I., Frise, E., Kaynig, V., Longair, M., Pietzsch, T., Preibisch, S., Rueden, C., Saalfeld, S., Schmid, B., et al. (2012). Fiji: an open-source platform for biological-image analysis. Nat. Methods *9*, 676–682.

Seah, C., Levy, M.A., Jiang, Y., Mokhtarzada, S., Higgs, D.R., Gibbons, R.J., and Bérubé, N.G. (2008). Neuronal death resulting from targeted disruption of the Snf2 protein ATRX is mediated by p53. J. Neurosci. 28, 12570–12580.

Sheng, M., and Kim, E. (2000). The Shank family of scaffold proteins. J. Cell Sci. 113, 1851–1856.

Shioda, N., Beppu, H., Fukuda, T., Li, E., Kitajima, I., and Fukunaga, K. (2011). Aberrant calcium/calmodulin-dependent protein kinase II (CaMKII) activity is associated with abnormal dendritic spine morphology in the ATRX mutant mouse brain. J. Neurosci. 31, 346–358.

Shioda, N., Yabuki, Y., Yamaguchi, K., Onozato, M., Li, Y., Kurosawa, K., Tanabe, H., Okamoto, N., Era, T., Sugiyama, H., et al. (2018). Targeting G-quadruplex DNA as cognitive function therapy for ATR-X syndrome. Nat. Med. 24, 802–813.

Siegert, S., Seo, J., Kwon, E.J., Rudenko, A., Cho, S., Wang, W., Flood, Z., Martorell, A.J., Ericsson, M., Mungenast, A.E., and Tsai, L.H. (2015). The schizophrenia risk gene product miR-137 alters presynaptic plasticity. Nat. Neurosci. 18, 1008–1016.

Soneson, C., Love, M.I., and Robinson, M.D. (2015). Differential analyses for RNA-seq: transcript-level estimates improve gene-level inferences. F1000Res. 4, 1521.

Spencer Noakes, T.L., Henkelman, R.M., and Nieman, B.J. (2017). Partitioning k-space for cylindrical three-dimensional rapid acquisition with relaxation enhancement imaging in the mouse brain. NMR Biomed. 30, 10.1002/nbm.3802.

Steadman, P.E., Ellegood, J., Szulc, K.U., Turnbull, D.H., Joyner, A.L., Henkelman, R.M., and Lerch, J.P. (2014). Genetic effects on cerebellar structure across mouse models of autism using a magnetic resonance imaging atlas. Autism Res. 7, 124–137.

Talpos, J.C., Winters, B.D., Dias, R., Saksida, L.M., and Bussey, T.J. (2009). A novel touchscreen-automated paired-associate learning (PAL) task sensitive to pharmacological manipulation of the hippocampus: a translational rodent model of cognitive impairments in neurodegenerative disease. Psychopharmacology (Berl.) 205, 157–168.

Tamming, R.J., Siu, J.R., Jiang, Y., Prado, M.A., Beier, F., and Bérubé, N.G. (2017). Mosaic expression of Atrx in the mouse central nervous system causes memory deficits. Dis. Model. Mech. 10, 119–126.

Tanaka, S., Ide, M., Shibutani, T., Ohtaki, H., Numazawa, S., Shioda, S., and Yoshida, T. (2006). Lipopolysaccharide-induced microglial activation induces learning and memory deficits without neuronal cell death in rats. J. Neurosci. Res. 83, 557–566.

Thomas, R.H., Chung, S.K., Wood, S.E., Cushion, T.D., Drew, C.J., Hammond, C.L., Vanbellinghen, J.F., Mullins, J.G., and Rees, M.I. (2013). Genotype-phenotype correlations in hyperekplexia: apnoeas, learning difficulties and speech delay. Brain 136, 3085–3095.

Thomas, K.T., Anderson, B.R., Shah, N., Zimmer, S.E., Hawkins, D., Valdez, A.N., Gu, Q., and Bassell, G.J. (2017). Inhibition of the Schizophrenia-Associated MicroRNA miR-137 Disrupts Nrg1α Neurodevelopmental Signal Transduction. Cell Rep. 20, 1–12.

Tronche, F., Kellendonk, C., Kretz, O., Gass, P., Anlag, K., Orban, P.C., Bock, R., Klein, R., and Schütz, G. (1999). Disruption of the glucocorticoid receptor gene in the nervous system results in reduced anxiety. Nat. Genet. 23, 99–103.

Tsien, J.Z., Chen, D.F., Gerber, D., Tom, C., Mercer, E.H., Anderson, D.J., Mayford, M., Kandel, E.R., and Tonegawa, S. (1996). Subregion- and cell type-restricted gene knockout in mouse brain. Cell 87, 1317–1326.

Tsutiya, A., Nakano, Y., Hansen-Kiss, E., Kelly, B., Nishihara, M., Goshima, Y., Corsmeier, D., White, P., Herman, G.E., and Ohtani-Kaneko, R. (2017). Human CRMP4 mutation and disrupted Crmp4 expression in mice are associated with ASD characteristics and sexual dimorphism. Sci. Rep. 7, 16812.

Ullmann, J.F., Watson, C., Janke, A.L., Kurniawan, N.D., Paxinos, G., and Reutens, D.C. (2014). An MRI atlas of the mouse basal ganglia. Brain Struct. Funct. 219, 1343–1353.

Vago, D.R., and Kesner, R.P. (2008). Disruption of the direct perforant path input to the CA1 subregion of the dorsal hippocampus interferes with spatial working memory and novelty detection. Behav. Brain Res. 189, 273–283.

Voineagu, I., Wang, X., Johnston, P., Lowe, J.K., Tian, Y., Horvath, S., Mill, J., Cantor, R.M., Blencowe, B.J., and Geschwind, D.H. (2011). Transcriptomic analysis of autistic brain reveals convergent molecular pathology. Nature 474, 380–384.

Vorhees, C.V., and Williams, M.T. (2006). Morris water maze: procedures for assessing spatial and related forms of learning and memory. Nat. Protoc. 1, 848–858.

Wang, W., Le, A.A., Hou, B., Lauterborn, J.C., Cox, C.D., Levin, E.R., Lynch, G., and Gall, C.M. (2018). Memory-Related Synaptic Plasticity Is Sexually Dimorphic in Rodent Hippocampus. J. Neurosci. 38, 7935–7951.

Watson, L.A., Solomon, L.A., Li, J.R., Jiang, Y., Edwards, M., Shin-ya, K., Beier, F., and Bérubé, N.G. (2013). Atrx deficiency induces telomere dysfunction, endocrine defects, and reduced life span. J. Clin. Invest. 123, 2049–2063.

Xu, J., Deng, X., Watkins, R., and Disteche, C.M. (2008). Sex-specific differences in expression of histone demethylases Utx and Uty in mouse brain and neurons. J. Neurosci. 28, 4521–4527.

Yi, L., Pimentel, H., Bray, N.L., and Pachter, L. (2018). Gene-level differential analysis at transcript-level resolution. Genome Biol. 19, 53.

Zerbino, D.R., Achuthan, P., Akanni, W., Amode, M.R., Barrell, D., Bhai, J., Billis, K., Cummins, C., Gall, A., Girón, C.G., et al. (2018). Ensembl 2018. Nucleic Acids Res. 46 (D1), D754–D761.

Zhao, L., Li, H., Guo, R., Ma, T., Hou, R., Ma, X., and Du, Y. (2013). miR-137, a new target for post-stroke depression? Neural Regen. Res. 8, 2441–2448.

Zhou, Y., Meng, P., Tang, B., Ke, Z., Liu, L., Chen, Y., and Zhu, F. (2019). MiR-616 promotes the progression of pancreatic carcinoma by targeting OXR1. Minerva Med. https://doi.org/10.23736/S0026-4806.19.06248-7.

STAR★METHODS

KEY RESOURCES TABLE

REAGENT or RESOURCE	SOURCE	IDENTIFIER
Antibodies		
anti-ATRX H-300	Santa Cruz Biotechnology, Inc	sc-15408
anti-NeuN	Millipore	MAB377; RRID:AB_2298772
anti-GFAP	Agilent Technologies, Inc	M0761; RRID:AB_2109952
;anti-IBA1	Wako Pure Chemical Corporation	019-19741; RRID:AB_839504
anti-INCENP	Sigma	I5283; RRID:AB_477113
anti-ATRX	Abcam	ab97508; RRID:AB_10680289
anti-H3K27me3	Millipore	07-449; RRID:AB_310624
anti-H3.3	Millipore	17-10245: RRID:AB_10953839
Normal rabbit IgG	Cell Signaling	2729S; RRID:AB_1031062
anti-Rabbit-HRP	Jackson ImmunoResearch Laboratories, Inc	111-036-003; RRID:AB_2337942
Bacterial and Virus Strains		
pmirGLO vector	Promega	E1330
PX459 plasmid (Addgene)	Ran et al., 2013	62988
Lenti-III-mico-GFP vector, viral titer > 10^7 IU/ml	Applied Biological Materials	MIMAT0000149
Chemicals, Peptides, and Recombinant Proteins		
XbaI	NEB	R0145S
BbsI	NEB	R0539S
Anti-miR miRNA Inhibitor; miR-137-3p	ThermoFisher	AM17000
KpnI	NEB	R0142S
Critical Commercial Assays		
SuperScript II Reverse Transcriptase	Invitrogen	18064022
miRVANA total RNA isolation kit	ThermoFisher	AM1560
TaqMan Advanced MicroRNA reverse transcription kit	ThermoFisher	A28007
TaqMan Universal PCR Master Mix, no AmpEraseTaqMan Universal PCR Master Mix, no AmpErase	ThermoFisher	4324018
Rapid GolgiStain Kit	FD Neurotechnologies, Inc	PK401
RNA 6000 Nano kit	Caliper Life Sciences	5067-1511
ScriptSeq Complete Gold Kit (H/M/R)	Illumina Inc.	BHMR1205
Deposited Data		
RNA sequencing of hippocampi from control and Atrx-cKO males and females	This study	GEO: GSE129975
Experimental Models: Cell Lines		
Neuro2A	ATCC	CCL-131
Experimental Models: Organisms/Strains		
Mouse: CaMKII-Cre: B6.Cg-Tg(Camk2a-cre)T29-1Stl/J	Jackson Laboratory	005359
Mouse: Atrx$^{fl/fl}$	Gift from Doug Higgs and Richard Gibbons	N/A
Oligonucleotides		
Oligonucleotides for qRT-PCR	Table S4	N/A
Oligonucleotides for sgRNA	Table S4	N/A
Oligonucleotides for ChIP-PCR	Table S4	N/A

Continued

REAGENT or RESOURCE	SOURCE	IDENTIFIER
Software and Algorithms		
Adobe Photoshop CS6	Adobe	RRID:SCR_014199;Version 13.0
OpenLab	Agilent	RRID:SCR_012158
Velocity 3D Image Analysis Software	PerkinElmer	RRID:SCR_002668; Demo Version 6.0.1
mni_autoreg tools	Collins et al., 1994	RRID:SCR_013621; http://www.bic.mni.mcgill.ca/software/mni_autoreg/
ANTS (advanced normalization tools)	Avants et al., 2011	RRID:SCR_004757; http://www.picsl.upenn.edu/ANTS/
FIJI	Schindelin et al., 2012	RRID:SCR_002285 https://fiji.sc
Prism 6.0	Graphpad	RRID:SCR_002798; https://www.graphpad.com
Simple Neurite Tracer	Longair et al., 2011	RRID:SCR_016566; https://imagej.net/Simple_Neurite_Tracer
ANY-Maze	Stoelting Co.	RRID:SCR_014289
cutadapt	Martin, 2011	RRID:SCR_011841; version 0.4.1
HISAT2	Kim et al., 2015	RRID:SCR_015530; version 2.0.4
SAMtools	Li et al., 2009	RRID:SCR_002105; http://www.htslib.org/
StringTie	Pertea et al., 2015	RRID:SCR_016323; v1.3.3; https://ccb.jhu.edu/software/stringtie/
tximport	Soneson et al., 2015	RRID:SCR_016752; https://bioconductor.org/packages/release/bioc/html/tximport.html
DESeq2	Love et al., 2014	RRID:SCR_015687; https://bioconductor.org/packages/release/bioc/html/DESeq2.html
pheatmap	Kolde, 2012	RRID:SCR_016418; https://cran.r-project.org/web/packages/pheatmap/index.html
Lancaster method	Yi et al., 2018	N/A
Other		
Bussey-Saksida mouse touch screen chambers	Lafayette Neuroscience	Model 80614-20

RESOURCE AVAILABILITY

Lead Contact
Further information and requests for resources and reagents should be directed to and will be fulfilled by the Lead Contact, Nathalie G. Bérubé (nberube@uwo.ca).

Materials Availability
All plasmids generated in this study are available upon request.

Data and Code Availability
The accession number for the RNA sequencing data reported in this paper can be accessed at GEO: GSE129975. Data analysis and graphical representations were performed using R scripts and publicly available packages as denoted in the methods detail section. All scripts are available upon request.

EXPERIMENTAL MODEL AND SUBJECT DETAILS

Mouse models
The *Atrx*^*loxP* mice have been described previously (Bérubé et al., 2005). *Atrx*^*loxP* mice were mated with C57BL/6 mice expressing Cre recombinase under the control of the *αCaMKII* gene promoter (Tsien et al., 1996). The progeny includes hemizygous male mice that produce no ATRX protein in forebrain excitatory neurons (*Atrx*-cKO). The *Atrx*-cKO males were mated to *Atrx*^*loxP* females to yield

homozygous deletion of *Atrx* in female mice (*Atrx*-cKO[Fem]). Male and female littermate floxed mice lacking the Cre allele were used as controls (Ctrl[Fem]). Genotyping of tail biopsies for the presence of the floxed and Cre alleles was performed as described previously (Bérubé et al., 2005). Mice were exposed to a 12-hour-light/12-hour-dark cycle and with water and chow *ad libitum*. Behavioral assessments were performed using male and female mice of 3 to 6 months of age, starting with less demanding tasks (open field tests, elevated plus maze) to more demanding ones (Morris water maze). ARRIVE guidelines were followed: mouse groups were randomized, experimenters were blind to the genotypes, and software-based analysis was used to score mouse performance in all the tasks. All behavioral experiments were performed between 9:00 AM and 4:00 PM. An analysis of the influence (or association) of sex on the hippocampal transcriptome and on several behaviors was performed. All procedures involving animals were conducted in accordance with the regulations of the Animals for Research Act of the province of Ontario and approved by the University of Western Ontario Animal Care and Use Committee (2017-048).

Cell lines
Neuro2a (ATCC® CCL131) male neuroblastoma cells were cultured in Eagle's Minimum Essential Medium (EMEM; Life Technologies), supplemented with 10% fetal bovine serum (FBS; Life Technologies) at 37°C and 5% CO_2 in a humidified incubator. The cells were confirmed to be negative for mycoplasma. Cell line authentication was not done.

METHOD DETAILS

Immunofluorescence staining
Mice were perfused with 25 mL phosphate buffered saline (PBS) followed by 25 mL 4% paraformaldehyde (PFA) in PBS and the brain fixed for 24 hours in 4% PFA in PBS and cryopreserved in 30% sucrose/PBS. Brains were flash frozen in Cryomatrix (Thermo Scientific) and sectioned at 8 μm thickness as described previously (Watson et al., 2013). For immunostaining, antigen retrieval was performed by incubating slides in 10 mM sodium citrate at 95°C for 10 min. Cooled sections were washed in PBS, permeabilized in 0.3% Triton X-100 and blocked with 10% normal goat serum (Sigma) for one hour. The slides were incubated overnight in primary antibody (ATRX: 1:200, NeuN: 1:200, GFAP: 1:200, IBA1: 1:500) diluted in 0.3% Triton-X/PBS. Sections were washed in 0.3% Triton-X/PBS 3x 5 min and incubated with secondary antibody (1:800) for one hour. Sections were washed again three times for 5 min, counterstained with DAPI and mounted with SlowFade Gold (Invitrogen). All images were captured using an inverted microscope (Leica DMI 6000b) with a digital camera (Hamamatsu ORCA-ER). Openlab image software was used for manual image capture, and images were processed using the Volocity software and Adobe Photoshop CS6. Cell counts of DAPI, GFAP, and IBA1 were performed in Adobe Photoshop. DAPI was counted per mm^2 and GFAP and IBA1 were counted as percentages of DAPI^{+} cells. One section from five pairs of Ctrl[Male]/*Atrx*-cKO[Male] was counted. Statistical significance was determined using an unpaired Student's t test.

Reverse transcriptase real-time PCR
Total RNA was isolated from control and *Atrx*-cKO frontal cortex and hippocampus using the miRVANA total RNA isolation kit (ThermoFisher) and reverse transcribed to cDNA using 1 μg RNA and SuperScript II Reverse Transcriptase (Invitrogen). Real-time PCR was performed in duplicate using gene-specific primers under the following conditions: 95°C for 10 s, 58°C for 20 s, 72°C for 30 s for 35 cycles. All data were normalized against β-actin expression levels. Total RNA was also used for reverse transcription of miRNA using the TaqMan Advanced MicroRNA reverse transcription kit (ThermoFisher). qRT-PCR was performed using the TaqMan Universal PCR Master Mix, no AmpErase (ThermoFisher) using advanced probes for miR-137-3p (mmu480924_mir), miR-34a-5p (mmu481304_mir), miR-27b-3p (mmu478270_mir), miR-485-5p (mmu482774_mir), and normalized to miR-191-5p (mmu481584_mir) under the following PCR conditions: 95°C for 10 min, 45 cycles of 95°C for 15 s and 60°C for 1 min. All primers are listed in Table S4.

Western blot analysis
Whole cell lysates were collected in standard RIPA buffer and quantified using a Bradford assay (BioRad). Protein lysates (50 μg) were loaded on a 6% SDS-PAGE gel and transferred to nitrocellulose membrane (BioRad) using a wet electroblotting system (BioRad). The membrane was blocked in 5% milk in Tris-buffered saline with 0.1% Tween-20 (SigmaAldrich) for 1 hour and incubated overnight at 4°C with primary antibody (ATRX: 1:500, INCENP: 1:3000). The following day the membrane was washed and incubated in the appropriate horseradish peroxidase-conjugated secondary antibody (1:4000). The membrane was rinsed briefly in enhanced chemiluminescence substrate (BioRad), exposed to film and quantified using ImageJ.

Magnetic resonance imaging
Mice were perfused with 30 mL of PBS supplemented with 1 μL/mL heparin (Sandoz) and 2mM ProHance (Bracco Imaging Canada) followed by 30 mL 4% paraformaldehyde supplemented with 2mM ProHance. After perfusion, mice were decapitated, and the skin, cartilaginous nose tip, and lower jaw were removed. The remaining brain and skull structures were incubated in PBS supplemented with 2 mM ProHance and 0.02% sodium azide for at least one month before MRI scanning (de Guzman et al., 2016). A multi-channel 7.0 Tesla MRI scanner (Agilent Inc., Palo Alto, CA) was used to image the brains within their skulls. Sixteen custom-built solenoid coils were used to image the brains in parallel (Nieman et al., 2018). In order to detect volumetric changes, we used the following

parameters for the MRI scan: T2- weighted, 3-D fast spin-echo sequence, with a cylindrical acquisition of k-space, a TR of 350 ms, and TEs of 12 ms per echo for 6 echoes, field-of-view equaled to $20 \times 20 \times 25$ mm3 and matrix size equaled to $504 \times 504 \times 630$. Our parameters output an image with 0.04 mm isotropic voxels. The total imaging time was 14 hours (Spencer Noakes et al., 2017).

MRI Registration and Analysis

To visualize and compare any changes in the mouse brains, the images are linearly (6 followed by 12 parameter) and non-linearly registered together. Registrations were performed with a combination of mni_autoreg tools (Collins et al., 1994) and ANTS (advanced normalization tools) (Avants et al., 2011). All scans are then resampled with the appropriate transform and averaged to create a population atlas representing the average anatomy of the study sample. The result of the registration is to have all images deformed into alignment with each other in an unbiased fashion. For the volume measurements, this allows for the analysis of the deformations needed to take each individual mouse's anatomy into this final atlas space, the goal being to model how the deformation fields relate to genotype (Lerch et al., 2008; Nieman et al., 2006). The jacobian determinants of the deformation fields are then calculated as measures of volume at each voxel. Significant volume differences can then be calculated by warping a pre-existing classified MRI atlas onto the population atlas, which allows for the volume of 182 different segmented structures encompassing cortical lobes, large white matter structures (i.e., corpus callosum), ventricles, cerebellum, brain stem, and olfactory bulbs (Dorr et al., 2008; Qiu et al., 2018; Richards et al., 2011; Steadman et al., 2014; Ullmann et al., 2014) to be assessed in all brains. Further, these measurements can be examined on a voxel-wise basis to localize the differences found within regions or across the brain. Multiple comparisons in this study were controlled for using the False Discovery Rate (Genovese et al., 2002).

Golgi staining and analysis

Brains from 3-month-old mice were stained using the FD Rapid GolgiStain Kit (FD Neurotechnologies, Inc). They were then flash frozen and sectioned on a cryostat at 100 μm thickness and further processed as per kit instructions. Hippocampal CA1 pyramidal neurons were imaged on a laser scanning confocal microscope (Leica SP5). z-Stacks were obtained of whole neurons (10-15 z-intervals per neuron). 65 Ctrl and 51 *Atrx*-cKO neurons were traced from 3 Ctrl/*Atrx*-cKO pairs. Dendrites were analyzed in ImageJ (FIJI) using the Simple Neurite Tracer plugin; the traces were analyzed using the Sholl plugin in ImageJ (FIJI) at a radius step size of 4 μm (Ferreira et al., 2014; Longair et al., 2011). Statistics were calculated by two-way repeated-measures ANOVA with Sidak's multiple comparison test or unpaired Student's t tests where applicable.

Transmission electron microscopy

Mice were perfused with 4% paraformaldehyde (VWR) dissolved in phosphate buffer and sectioned at 500 μm on a Vibratome Series 1000 Sectioning System. Sections were post-fixed overnight in 4% paraformaldehyde for 24h and in 1% glutaraldehyde for 1 hour, then washed and left in phosphate buffer until preparation of ultra-thin sections. Slices were transferred to the Biotron facility at Western University for the remaining steps. Coronal slices from the hippocampal layer were rinsed in distilled water, post-fixed for one hour at room temperature in 1% osmium tetroxide (Electron Microscopy Sciences Warrington, PA) and 1.5% potassium ferrocyanide and post-fixed for a second hour in 1% osmium tetroxide (Harris et al., 1992). The slices were quickly dehydrated through a graded series of ethanol, rinsed in 100% acetone and then infiltrated with inversion for one hour in 50% epon-araldite resin and placed overnight in 100% resin on a rotator. The slices were polymerized overnight at 60°C in a vented oven, sandwiched between two sheets of Aclar film covered with a light weight (Bisht et al., 2016). The hippocampal region was cut from the resin-embedded slice using a razor blade and mounted on a blank epoxy block using cyanoacrylate glue. Semi-thin sections were made with a Reichert Ultracut ultramicrotome and stained with toluidine blue and used to select the CA1 neuropil region for ultrathin sectioning. Thin sections (100 nm) were collected on 200 mesh nickel grids (EMS), post-stained with lead citrate and images were collected with a Philips 420 transmission electron microscope equipped with an AMT 4K megapixel XR41S-B camera (Woburn, MA). Images were captured within the stratum radiatum / stratum lacunosum moleculare at 9200X in a semi-random manner to obtain at least 50 synapses containing a distinct synaptic cleft without regard to the length of the cleft. Image analysis was performed in ImageJ. A total of 104 Ctrl[Male] and 84 *Atrx*-cKO[Male] synapses were quantified from 3 Ctrl[Male] and 3 *Atrx*-cKO[Male] mice. Synapses were binned in 50 nm increments from the active zone and the number of docked vesicles and vesicles in each bin were counted; this also determined total number of vesicles per synapse. Vesicle cluster size was measured to calculate vesicle density. The area of the post-synaptic density was also quantified. Statistics were calculated by two-way repeated-measures ANOVA with Sidak's multiple comparison test or unpaired Student's t tests where applicable.

Open field test

In the open field test, locomotor activity was automatically recorded (AccuScan Instrument). The mice were placed in an arena with an area of 20 cm x 20 cm with 30 cm high walls. Mice were acclimated to the room for ten minutes prior to testing. Locomotor activity was measured in 5 min intervals over 2 hours as previously described (Tamming et al., 2017). Distance traveled and time spent in the center were recorded. Statistics were calculated by two-way repeated-measures ANOVA with Sidak's multiple comparison test or unpaired Student's t tests where applicable.

Elevated plus maze

Animals were placed in the center of the elevated plus maze (Med Associate Inc) and their activity was recorded over 5 min. Total time spent in the open and closed arms was recorded using computer software (AnyMaze). The center of the mouse body was used as an indicator of which zone they were in. Statistics were calculated by unpaired Student's t tests.

Y maze test

Animals were placed in the center of a symmetrical three-armed Y maze as described (de Castro et al., 2009; Tamming et al., 2017). Each mouse underwent one trial of 5 minutes. Order of arm entry was recorded using computer software (AnyMaze) and spontaneous alternation was counted when a mouse entered all three arms in a row without visiting a previous arm.

Novel object recognition task

Mice were habituated in an open arena with no objects for 5 minutes on Day 1 and Day 2, as described (Tamming et al., 2017). On Day 3, mice were exposed to two identical objects for ten minutes (A; a red plastic ball attached on top of a yellow cube base). Video tracking (AnyMaze) was used to record time spent with each object. To test short-term memory, mice were exposed to the original object (A) and a novel object (B; a blue plastic pyramid attached on top of a green prism base) 1.5 hours after training. To test long-term memory, mice were exposed to (A) and (B) 24 hours after training. Novel object recognition was expressed as the percentage of time spent with the novel object as a fraction of the total time spent interacting. Interaction was defined as sniffing or touching the object, but not leaning against or climbing on the object.

Morris water maze

The Morris water maze was conducted as described previously (Vorhees and Williams, 2006). The task was performed in a 1.5 m diameter pool with 25°C water and the platform was submerged 1 cm beneath the water surface. Spatial cues (shapes printed in black & white) were distributed around the pool. Mice were given four trials (90 s) a day for 4 consecutive days with a 15 min intertrial period. The latency, distance, and swim speed to find the platform was recorded using video tracking software (AnyMaze). If the mice did not find the platform within 90 s, they were gently guided onto the platform. On the fifth and the twelfth days the platform was removed, and time spent in each quadrant of the maze was recorded using the video software. Statistics were calculated by one- or two-way repeated-measures ANOVA with Sidak's multiple comparison test, where applicable.

Contextual fear conditioning

To measure contextual fear memory, mice were placed in a 20 cm x 10 cm clear acrylic enclosure with a metal grid floor and one wall distinct from the others (stripes were drawn on one of the walls). The chamber was equipped with an electric shock generator. Videos were recorded using the AnyMaze video tracking software. On Day 1, mice could explore the enclosure freely and at 150 s the mice were given a shock (2 mA, 180 V, 2 s). After 30 s, the mice were returned to their home cage. The next day (24 h), the mice were placed back into the enclosure for 6 min and freezing time was measured in 30 s intervals. Freezing was defined as immobility lasting more than 0.5 s. Statistics were calculated by two-way repeated-measures ANOVA with Sidak's multiple comparison test or unpaired Student's t tests where applicable.

Touchscreen assays

The paired associate learning (dPAL) and visual paired discrimination (VPD) and reversal tasks were performed as previously described (Bussey et al., 2008; Delotterie et al., 2015; Talpos et al., 2009). Animals were food-restricted to 85% starting body weight. Animals were separated into two counter-balanced subgroups to control for time of day of testing, and equipment variation. Mice were tested in Bussey-Saksida mouse touch screen chambers (Lafayette Neuroscience) with strawberry milkshake given as a reward. For the dPAL acquisition phase, animals were tested for their ability to associate objects with locations. Mice were presented with two images in two of three windows; one image was in its correct location (S+) and one was in one of its two incorrect locations (S-). The third window was blank. A correct response triggered reward presentation and start of an inter-trial period. The pre-training was repeated until mice reached criterion (completion of 36 trials within 60 minutes). The dPAL evaluation phase was performed for 45 sessions over 9 weeks. A correct response triggered reward presentation, whereas an incorrect response caused a 5 s time out and the house lights to turn on. An incorrect response also resulted in a correction trial, where the same S+/S- images were presented in the same two locations until the mouse responded correctly. The mouse was given 36 trials over 60 minutes per day. Percent correct, number of correction trials, latency to a correct or incorrect response, and latency to retrieve reward were recorded for each week.

VPD acquisition required the animal to touch the same image (S+) no matter which window it appeared in. The other screen had an incorrect image (S-). A correct response triggered reward presentation, whereas an incorrect response triggered the house lights to turn on, a time out of 5 s, and a correction trial to begin (previous trial repeated until a correct choice is made). This was repeated until mice reached criterion of 24/30 trials correct within 60 minutes over 2 consecutive days, after which baseline measurements were done for two sessions. Parameters for baseline were identical to the acquisition steps. Immediately following baseline measurements, the VPD task reversal began, where most parameters were the same as the acquisition, but the correct image associated with the reward was S-, and the incorrect response that triggers house lights was S+. The mouse was given 30 trials per day over

10 days. Percent correct, number of correction trials needed, latency to a correct or incorrect response, and latency to retrieve reward on each day were recorded. Statistics were calculated by two-way repeated-measures ANOVA with Sidak's multiple comparison test or unpaired Student's t tests where applicable.

RNA sequencing

Hippocampal total RNA was isolated using the miRVANA RNA isolation kit (ThermoFisher) from three pairs of 3-month-old $Ctrl^{Male}$, $AtrxcKO^{Male}$, $Ctrl^{Fem}$ and $AtrxcKO^{Fem}$ mice (12 samples total). RNA was quantified using the Qubit 2.0 Fluorometer (Thermo Fisher Scientific, Waltham, MA) and quality was assessed using the Agilent 2100 Bioanalyzer (Agilent Technologies Inc., Palo Alto, CA) with the RNA 6000 Nano kit (Caliper Life Sciences, Mountain View, CA). Libraries were prepared, including rRNA reduction, using the ScriptSeq Complete Gold Kit (H/M/R) (Illumina Inc., San Diego, CA). Samples were fragmented, cDNA was synthesized, tagged, cleaned-up and subjected to PCR with barcoded reverse primers (ScriptSeq Index PCR Primers) to permit equimolar pooling of samples into one library. The pooled library size distribution was assessed with an Agilent High Sensitivity DNA Bioanalyzer chip and quantitated using the Qubit 2.0 Fluorometer. All samples were sequenced at the London Regional Genomics Centre (Robarts Research Institute, London, Ontario, Canada; http://www.lrgc.ca) using the Illumina NextSeq 500 (Illumina Inc., San Diego, CA). The libraries were sequenced as a paired end run, 2 x76 bp, using a High Output v2 kit (150 cycles). Fastq data files were downloaded from BaseSpace. At least 60 million fragments were obtained for each sample. Raw reads were pre-processed with the sequence-grooming tool cutadapt (Zerbino et al., 2018) version 0.4.1 with the following quality trimming and filtering parameters ('–phred33–length36 -q 5–stringency 1 -e 0.1'). Each set of paired-end reads was mapped against the *Mus musculus* GRCm38.p6 primary assembly downloaded from Ensembl (Pertea et al., 2015) release 94 (https://useast.ensembl.org/Mus_musculus/Info/Annotation) using HISAT2 version 2.0.4. SAMtools was then used to sort and convert SAM files. The read alignments and *Mus musculus* GRCm38 genome annotation were provided as input into StringTie v1.3.3 (Soneson et al., 2015) which returned gene and transcript abundances for each sample. We imported coverage and abundances for transcripts into R using the tximport (Love et al., 2014) R package and conducted differential analysis of transcript count data stratified or not on sex using the DESeq2 R package. We use the independent hypothesis weighting (IHW) Bioconductor package (Ignatiadis et al., 2016) to weight p values and adjust for multiple testing using the procedure of Benjamini Hochberg (BH) (Benjamini and Hochberg, 1995). We first identified transcripts associated with ATRX loss in male and female independently (ie stratified analysis). For the unstratified analysis, an interaction term was added to the model to test if the effect of *Atrx* deletion differs according to sex. K-means clustering based on Euclidean distance was used to cluster significant transcripts in four groups. Clustering and heatmap visualization were conducted using the pheatmap R package. To further investigate the association between ATRX loss and expression of miR137 targets, we curated the literature to list 3,512 genes and tested association of the expression of the corresponding transcripts with the sex*genotype interaction term as described above using DESeq2 R/Bioconductor package. Transcripts p values were then aggregated using the Lancaster method (Yi et al., 2018).

Generation of ATRX knockout cell line by CRISPR Cas9

Two single-guide RNA (sgRNA1 and sgRNA2) sequences targeting two loci in exon 9 of the mouse *Atrx* gene were designed by using the CRISPR design tool (https://www.benchling.com/crispr/). Pairs of DNA oligonucleotides harboring sgRNA1 and sgRNA2 sequences (Table S4) were individually annealed and ligated into the BbsI (NEB) site of the PX459 plasmid (Addgene #62988) as previously described by Ran et al. (2013). After gRNA1 and gRNA2 cloning into PX459 plasmid, a dual-guide RNA (gRNA1+gRNA2) cassette was assembled on the gRNA1-containing PX459 plasmid. Briefly, the gRNA2-containing cassette (U6 promoter-gRNA2-gRNA scaffold) was amplified and inserted into XbaI (NEB) and KpnI (NEB) sites of gRNA1-containing PX459 plasmid. Neuro2A cells were transfected with dual-guide RNA containing PX459 plasmid by Lipofectamine 3000 (ThermoFisher), according to the manufacturer's instructions. Transfected cells were selected with Puromycin (2µg/ml) for 3-5 days and then diluted to obtain the individual clones.

Chromatin immunoprecipitation

Neuro2A and Neuro2A-ATRXKO cells were grown in DMEM for 48 hours, collected in 10mL DMEM and crosslinked in 1% formaldehyde. The cells were lysed in SDS buffer and sonicated. Immunoprecipitation was performed with the following antibodies: anti-ATRX (Abcam, ab97508), anti-H3K27me3 (Millipore, 07-449), anti-H3.3 (Millipore, CS207327). Rabbit IgG (Cell Signaling) was used as a control. Input samples represent 1/25 of total chromatin input. Real-time PCR experiments were conducted as follows: 95°C for 5 min, 40 cycles of 95°C for 10 s, 60°C for 20 s, and 72°C for 30 s. This procedure was repeated in triplicate. Primers used to amplify the P1-P4 regions are listed in Table S4.

Dual-luciferase reporter assay

Several reporter plasmids were constructed containing the putative target sequence for miR-137 identified in the *Cacna1g*, *Glrb*, *Synpo*, *Huwe-1* and *Adcyap1r1* 3'UTR. For *Glrb*, we also constructed a reporter plasmid with a mutant form of the target site. Neuro2A cells were infected with a lenti-GFP mmu-miR-137-3p miRNA virus (Lenti-III-mico-GFP vector, viral titer > 10^7 IU/ml, miRNA ID: MIMAT0000149; Applied Biological Materials; abm, Vancouver, Canada) 48 hours before transfection with the reporter plasmids in the presence or absence of 80nM miR-137 inhibitor (Anti-miR miRNA Inhibitor, Thermofisher Scientific). The cells were collected and

lysed 48 hours later and luciferase activity was detected using a Dual-LuciferaseR Reporter Assay System kit (E1910, Promega Corporation, Madison, WI, USA). The ratio of firefly luciferase to renilla luciferase was regarded as relative luciferase activity.

QUANTIFICATION AND STATISTICAL ANALYSIS

Data collection and analyses were performed blind to the conditions of the experiment. Sample sizes were not pre-determined and similar to those reported in the literature. For MRI and behavior experiments, 'n' refers to number of separate mice. All data were analyzed using GraphPad Prism software with Student's t test (unpaired, two-tailed) or one-way ANOVA for experiments with one variable or two-way repeated-measures ANOVA with post hoc test for experiments with two variables. All results are depicted as mean ± SEM unless indicated otherwise. P values of less than 0.05 were considered to indicate significance. All statistical details are outlined in the Method Details section and in the figure legends.